

The geodynamics of collision of a microplate (Chilenia) in Devonian times deduced by the pressure–temperature–time evolution within part of a collisional belt (Guarguaraz Complex, W-Argentina)

Arne P. Willner · Axel Gerdes · Hans-Joachim Massonne · Alexander Schmidt · Masafumi Sudo · Stuart N. Thomson · Graciela Vujovich

Received: 30 May 2010/Accepted: 16 November 2010
© Springer-Verlag 2010

Abstract The Guarguaraz Complex in West Argentina formed during collision between the microplate Chilenia and South America. It is composed of neritic clastic metasediments with intercalations of metabasic and ultrabasic rocks of oceanic origin. Prograde garnet growth in metapelite and metabasite occurred between 1.2 GPa, 470°C and 1.4 GPa, 530°C, when the penetrative s_2 -foliation was formed. The average age of garnet crystallization of

Communicated by T. L. Grove.

Electronic supplementary material The online version of this article (doi:[10.1007/s00410-010-0598-8](https://doi.org/10.1007/s00410-010-0598-8)) contains supplementary material, which is available to authorized users.

A. P. Willner (✉)
Institut für Geologie, Mineralogie und Geophysik,
Ruhr-Universität, 44780 Bochum, Germany
e-mail: arne.willner@rub.de

A. P. Willner · H.-J. Massonne
Institut für Mineralogie und Kristallchemie,
Universität Stuttgart, Azenbergstr. 18, 70174 Stuttgart, Germany

A. Gerdes
Institut für Geowissenschaften, Mineralogie,
J.W. Goethe Universität, 60438 Frankfurt, Germany

A. Schmidt · M. Sudo
Institut für Erd- und Umweltwissenschaften,
Universität Potsdam, Karl-Liebknechtstr. 24, 14476 Golm,
Germany

S. N. Thomson
Department of Geosciences, University of Arizona,
1040E, 4th Street, Tucson, AZ 85721-0077, USA

G. Vujovich
Laboratorio Tectónica Andina, FCEyN, Universidad de Buenos Aires/CONICET, Pabellón II, Ciudad Universitaria,
1428 Buenos Aires, Argentina

390 ± 2 Ma (2σ) was determined from three four-point Lu–Hf mineral isochrones from metapelite and metabasite samples and represents the time of collision. Peak pressure conditions are followed by a decompression path with slight heating at 0.5 GPa, 560°C. Fluid release during decompression caused equilibration of mineral compositions at the rims and also aided Ar diffusion. An $^{40}\text{Ar}/^{39}\text{Ar}$ plateau age of white mica at 353 ± 1 Ma (1σ) indicates the time of cooling below 350–400°C. These temperatures were attained at pressures of 0.2–0.3 GPa, indicative of an average exhumation rate of ≥ 1 mm/a for the period 390–353 Ma. Late hydrous influx at 0.1–0.3 GPa caused pervasive growth of sericite and chlorite and reset the Ar/Ar ages of earlier coarse-grained white mica. At 284–295 Ma, the entire basement cooled below 280°C (fission track ages of zircon) after abundant post-collisional granitoid intrusion. The deeply buried epicontinental sedimentary rocks, the high peak pressure referring to a low metamorphic geotherm of 10–12°C/km, and the decompression/heating path are characteristics of material buried and exhumed within a (micro) continent–continent collisional setting.

Keywords Albite–amphibolite facies · Geothermobarometry · Lu–Hf system · K–Ar system · Fission track (zircon) · Collision zone · Garnet · Potassic white mica

Introduction

The growth of continental crust at the Pacific margin at latitudes 30°–40°S in Phanerozoic times (Fig. 1a) involved the formation of accretionary prisms, juvenile magmatic additions and collision of allochthonous terranes (e.g. Ramos 2000, 2009; Willner et al. 2008). Whereas the nature of the

Argentine Precordillera as an allochthonous microplate called Cuyania is well established in spite of contrasting proposals about its derivation (Ramos 2000, 2009), the existence of a further allochthonous terrane to the west is still a matter of debate. Ramos et al. (1986) proposed a separate “Chilenia” terrane mainly due to the occurrence of ultrabasic bodies within a metamorphic belt in the Frontal Cordillera and western Precordillera of Argentina. These were interpreted as remnants of ophiolites along a suture. However, surface exposures of rocks of Chilenia itself have not yet been firmly proven to be exposed outside the proposed suture zone, although there is indirect evidence for a separate microplate from chemical fingerprints in magmatites (e.g. Mpodozis and Kay 1992). New evidence for its existence and evolution can be derived by unravelling the geodynamic evolution of two contrasting metamorphic belts with high-pressure (HP) rocks on both sides of the proposed terrane (Fig. 1a): (1) the Guarguaraz Metamorphic Complex at the suture between Cuyania and Chilenia in W Argentina (longitude 69°W) has characteristics of a Palaeozoic collision zone (Massonne and Calderón 2008; Willner et al. 2008), whereas (2) the basement of the Coastal Cordillera in central Chile (longitude 72°W) represents a Late Palaeozoic coastal accretionary prism (e.g. Hervé 1988, Willner 2005, Willner et al. 2005; Glodny et al. 2005; Richter et al. 2007). Yet both HP complexes are composed of continent-derived metasediments including up to 10–15% intercalations of disrupted oceanic crust. A comparison of the evolution of these similar complexes with contrasting settings will aid in the understanding of collision zones particularly of microplates in general.

The purpose of this paper is to explore the pressure–temperature–time evolution of the Guarguaraz Complex in more detail by a combined multimethod geothermobarometric and geochronological approach for a better understanding of processes of terrane collision and their recognition in general. We will study phase relations of the HP part of the amphibolite facies, unravel specific PT conditions and evolutions typical for a collisional setting as well as derive a more exact timing of the collision and the duration of processes like exhumation. This is the first time such a detailed multimethod approach has been applied in the Andes, and thus, our results should help to better define other similar microplate collisional settings apparent in the classical continental margin orogen of the Andes (Ramos 2009).

Geological setting

The westernmost exposures of metamorphic basement rocks in Argentina that include ultrabasic rocks, occur

within the Frontal Cordillera and the western flank of the Precordillera. Two units can be distinguished in the southern part (Caminos 1993): a low-grade unit in the north (Davis et al. 1999, 2000; Gerbi et al. 2002) and a medium-grade unit in the south (Polanski 1964, 1972; Bjerg et al. 1990; Lopez and Gregori 2004) known as the Guarguaraz Complex (Fig. 1b). This Complex consists of following four main lithologies with protolith interpretations derived from geochemical studies (Bjerg et al. 1990; Lopez and Gregori 2004; Lopez et al. 2009; Fig. 1c): (1) garnet–micaschist and quartzitic schist dominate the metamorphic basement and are considered as originally derived through erosion of a mature cratonic continental basement. The metasediments contain intercalated lenses of (2) garnet-bearing amphibolite with a N- or E-MORB geochemical signature, (3) serpentinite with tremolite-/talc-bearing wall-rocks and (4) marbles and calc-silicate. Massonne and Calderón (2008) studied a metapelite and derived a PT path characterized by HP metamorphism at 1.35 GPa, 500°C followed by a decompression to mid-crustal conditions at 0.8 GPa, 565°C. These authors were the first to propose a collisional setting based on their PT data. An earlier peak PT estimate at 0.9 ± 0.2 GPa, 500 ± 50 °C on amphibolite corresponds to a midcrustal stage only (Ruviños et al. 1997).

Detrital zircon U–Pb ages reveal a maximum depositional age for the Guarguaraz metasedimentary rocks of 563 Ma (Willner et al. 2008). This is consistent with findings of acritarchae of a presumed Vendian-Cambrian age in the metasediments (Lopez et al. 2009) and a whole-rock Sm–Nd isochron age of 655 ± 76 Ma for the intercalated metabasite interpreted as the crystallization age of the protolith (Lopez et al. 2009). Furthermore, the 563-Ma age is consistent with a protolith age of 576 ± 17 Ma (U–Pb zircon) reported from a metabasite in the low-grade Cortaderas Complex further north (Davis et al. 2000).

The detrital zircon age spectrum resembles that of Early Palaeozoic sedimentary rocks of the Precordillera and displays positive ϵ Hf values that follow a Mid-Proterozoic crustal evolution trend starting at 1.2–1.5 Ga with juvenile magma production (Willner et al. 2008). This is consistent with Sm–Nd model ages at 1.4–1.7 Ga for the Guarguaraz micaschist (Basei et al. 1998), whereas model ages for the metabasite are at ~ 1 Ga (Lopez et al. 2009). Previous records of the age of metamorphism are defined only by a poor Rb–Sr whole-rock isochron of the Guarguaraz micaschist at 375 ± 34 Ma (Basei et al. 1998) and a K–Ar whole-rock age of 370 ± 18 Ma by Caminos et al. (1979). In the low-grade units to the north of the Guarguaraz Complex, Davis et al. (1999) published $^{40}\text{Ar}/^{39}\text{Ar}$ plateau ages of 384 ± 0.5 Ma and 377 ± 0.5 Ma from undefined white-mica concentrates interpreted as crystallization ages dating the peak of low-grade metamorphism.

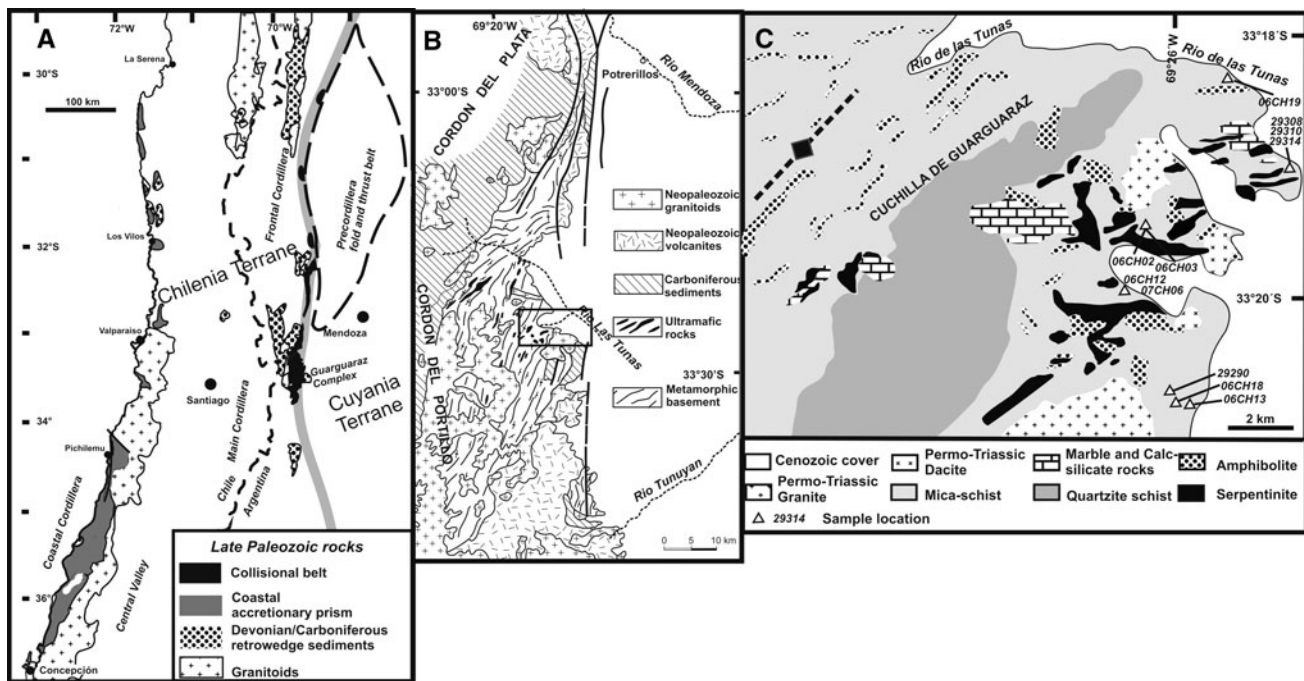


Fig. 1 **a** Compilation of tectonic environments during late Palaeozoic times at lat. 29–37°S based on Caminos (1979), Mpodozis and Kay (1992), Ramos (2000), and Willner et al. (2005). The light grey line marks the suture between the Chilenia and Cuyania Terranes according to Ramos (2000). **b** Simplified geological map of the

southern part of the Argentine Frontal Cordillera at 33°10'S–33°45'S according to Polanski (1964, 1972). **c** Detailed lithological map of the Guararaz Complex south of the Rio de las Tunas according to Lopez and Gregori (2004)

All rocks are overprinted by a penetrative NE-trending second transposition foliation that is subparallel to the bedding and to relicts of a first foliation. The regional stretching lineation strikes NW–SE. The transposition foliation is deformed to NE–SW-trending mega-anticlines (Fig. 1b, c; Lopez and Gregori 2004). Granodioritic-tonalitic magmas intruded the basement at 348 ± 35 Ma (Rb–Sr) and 337 ± 15 Ma (K–Ar) as dated by Caminos et al. (1979). Astini et al. (2009) also mentioned bimodal volcanism at 360–336 Ma in the Western Sierras Pampeanas that is interpreted as post-collisional magmatism and related to extension. The Guararaz basement is unconformably overlain by Upper Carboniferous sediments (El Plata Formation). Siliciclastic Devonian and Carboniferous sedimentary rocks constitute an extensive basin of siliciclastic sediments to the west of the Argentine Precordillera (Caminos 1979). The Carboniferous sedimentary rocks and the basement were intruded by Permo-Triassic granitoids (264–202 Ma) and are overlain by Permo-Triassic andesitic and rhyolitic lavas of the Choiyoi Group formed during major crustal extension (Gregori et al. 1996). Late Palaeozoic intrusions caused wide contact metamorphic halos discernable by the blastesis of andalusite (Vujovich and Gregori 2002).

Petrographic characteristics and mineral composition

For the study of PT conditions and age dating, we concentrated on two abundant rock types only: garnet–micaschist and garnet–amphibolite (Fig. 1). The mineral assemblages as well as their locations are given in Table 1. Structural formulae of representative analyses used for PT calculations are presented in Table 2. Further data are available as supplementary data tables which can be downloaded from electronic supplementary material and upon request to the first author. Abbreviations of minerals and end-member components in this paper are as follows: Ab = albite, Am = amphibole, Bt = biotite, Cl = chlorite, Ep = epidote, Gt = garnet, Im = ilmenite, Kf = potassic feldspar, Lw = lawsonite, Mt = magnetite, Pg = paragonite, Pl = plagioclase, Qz = quartz, Rt = rutile, Tt = titanite, V = H_2O as hydrous fluid, Wm = potassic white mica.

Garnet–micaschist

The mineral assemblage of the metapsammopelitic rock is garnet – chlorite – biotite – white mica – ilmenite – plagioclase \pm epidote \pm rutile \pm K-feldspar \pm titanite \pm magnetite (Table 1). The prominent fabric is a penetrative s_2 transposition foliation defined by an alternating

Table 1 Assemblages

Sample	Amphibole	Garnet	Epidote	Chlorite	White mica	Biotite	Quartz	Albite	Plagioclase	K-feldspar	Rutile	Ilmenite	Titanite	Magnetite	Andalusite									
<i>Metapelite</i>																								
29290	x	x	x	x	x	x	x	x	x	x	x	x	x	x	x									
06CH02	x	x	x	x	x	x	x	x	x	x	x	x	x	x	x									
06CH12	x	x	x	x	x	x	x	x	x	x	x	x	x	x	x									
06CH03	x	x	x	x	x	x	x	x	x	x	x	x	x	x	x									
06CH19	x	x	x	x	x	x	x	x	x	x	x	x	x	x	x									
06CH27	x	x	x	x	x	x	x	x	x	x	x	x	x	x	x									
06CH18 ^a	x	x	x	x	x	x	x	x	x	x	x	x	x	x	x									
<i>Metabasite</i>																								
06CH13	x	x	x	x	x	x	x	x	x	x	x	x	x	x	x									
07CH06	x	x	x	x	x	x	x	x	x	x	x	x	x	x	x									
29310	x	x	x	x	x	x	x	x	x	x	x	x	x	x	x									
29314	x	x	x	x	x	x	x	x	x	x	x	x	x	x	x									
29308	x	x	x	x	x	x	x	x	x	x	x	x	x	x	x									
Sample	Conditions P [GPa], T [°C]			Lu/Hf age [Ma]			Ar/Ar age [Ma]			FT age [Ma]			Location											
<i>Metapelite</i>																								
29290	1.31/1463	1.42/532	0.5/543	388.3 ± 1.7	352.7 ± 0.6	White mica			Zircon			Stream W' Refugio Don Domingo			33°21'04"									
06CH02	1.26/475	1.45/563	0.40/582									Road NW' Refugio El Condor			33°19'40.7"									
06CH12												Road 2 km S' Mina 12 Hermanos			33°19'57"									
06CH03												Road NW' Refugio El Condor			33°19'48.4"									
06CH19												Creek W' Refugio La Plaza			33°18'35.4"									
06CH27												Arroyo Grande/Refugio Scaravelli			33°36'38.2"									
06CH18 ^a												Road SE' Refugio Don Domingo			33°21'06.8"									
<i>Metabasite</i>																								
06CH13												Road E' Refugio Don Domingo			33°21'11.1"									
07CH06	1.28/480	1.36/495	389.9 ± 2.4									Road 2 km S' Mina 12 Hermanos			33°19'57"									
29310	1.13/495	1.42/592	0.41/555									Hill 2 km S' Refugio La Plaza			33°19'10.7"									
29314												Hill 2 km S' Refugio La Plaza			33°19'10.7"									
29308												Hill 2 km S' Refugio La Plaza			33°19'10.7"									
Coordinates																								
Lat. (S)																								
Long. (W)																								

^a For this rock, a maximum deposition age of 563 Ma (U/Pb zircon) was derived by Willner et al. (2008)

Table 2 Representative mineral analyses and mineral compositions calculated with PERPLE_X for comparison

Garnet ^a	Metapsammopelite						Metapsammopelite					
	29290 I Core	Calc. 490°C 1.15 GPa	29290 II Rim	Calc. 510°C 1.25 GPa	29290 III o. rim	Calc. 550°C 0.6 GPa	06CH02 I Core	06CH02 II Rim	06CH02 III o. rim	06CH12 I Core	06CH12 II Rim	
Si	5.913	6.000	5.930	6.000	5.921	6.000	5.995	6.011	5.999	5.941	5.979	
Alt	0.087		0.070		0.079		0.005		0.001	0.059	0.021	
Sum	6.000		6.000		6.000		6.011		6.000	6.000	6.000	
Alo	3.827	4.000	3.893	4.000	3.946	4.000	3.686	3.734	3.830	3.684	3.822	
Fe ³⁺	0.148		0.097		0.046		0.295		0.246	0.164	0.168	
Ti	0.025		0.010		0.009		0.018		0.020	0.006	0.010	
Sum	4.000		4.000		4.000		4.000		4.000	4.000	4.000	
Fe ²⁺	2.420	2.200	3.563	2.620	3.407	3.300	2.605	2.827	2.433	2.106	3.147	
Mn	2.122	1.680	0.654	1.020	1.500	1.080	2.306	1.863	2.171	2.607	1.793	
Ca	1.372	2.000	1.555	2.120	0.727	1.200	0.847	1.009	0.953	1.187	0.826	
Mg	0.117	0.120	0.257	0.240	0.402	0.420	0.228	0.263	0.434	0.118	0.236	
Sum	6.031	6.000	6.030	6.000	6.035	6.000	5.987	5.962	5.991	6.017	6.001	
Xand	0.025		0.016		0.008		0.049		0.041	0.027	0.028	
Xgross	0.203	0.333	0.242	0.353	0.113	0.200	0.092	0.128	0.132	0.148	0.110	
Xspes	0.352	0.280	0.109	0.170	0.249	0.180	0.385	0.313	0.362	0.433	0.299	
Xpyr	0.019	0.020	0.043	0.040	0.067	0.070	0.038	0.044	0.072	0.020	0.039	
Xalm	0.401	0.367	0.591	0.437	0.565	0.550	0.435	0.474	0.406	0.350	0.524	
XMg	0.046	0.052	0.067	0.084	0.106	0.113	0.081	0.085	0.151	0.053	0.070	
Garnet ^a	Metabasite						Metabasite					
Stage Generation	07CH06 II Rim	Calc. 500°C 1.1 GPa	07CH06 I Core	Calc. 550°C 1.1 GPa	07CH06 III Core	Calc. 550°C 0.6 GPa	29310 I Core	29310 II Rim	29310 III o. rim	29314 I Core	29314 II Rim	
Si	5.834	6.000	5.789	6.000	6.000	6.000	5.909	5.928	5.921	5.877	5.900	
Alt	0.166		0.211		0.091		0.072		0.079	0.123	0.100	
Sum	6.000		6.000		6.000		6.000		6.000	6.000	6.000	
Alo	3.915	4.000	3.859	4.000	4.000		3.778	3.868	3.898	3.650	3.951	
Fe ³⁺	0.077		0.121				0.213	0.126	0.093	0.313	0.046	
Ti	0.007		0.020				0.009	0.006	0.009	0.037	0.004	
Sum	4.000		4.000				4.000	4.000	4.000	4.000	4.000	
Fe ²⁺	3.829	2.700	2.900	3.440	2.920		2.694	3.511	3.205	1.337	3.780	
Mn	0.241	0.600	1.039	0.240	1.200		1.929	1.106	1.267	3.504	0.826	
Ca	1.754	2.620	2.041	2.100	1.580		1.194	1.065	1.212	1.119	1.050	
Mg	0.254	0.080	0.111	0.220	0.300		0.208	0.335	0.346	0.076	0.389	
Sum	6.079	6.000	6.092	6.000	6.000		6.024	6.017	6.029	6.037	6.044	

Table 2 continued

Garnet ^a	Metabasite						29310						29314		
Stage	07CH06			Calc. 500°C 1.1 GPa			07CH06			Calc. 550°C 1.1 GPa			1	II	III
Generation	Rim	Core	Core	Core	Core	Core	Core	Core	Core	Core	Core	Core	Core	Core	Rim
Xand	0.013			0.020						0.035			0.021		0.016
Xgross	0.276	0.437	0.315		0.350		0.263		0.163		0.156		0.186		0.134
Xspes	0.040	0.100	0.171		0.040		0.200		0.320		0.184		0.210		0.581
Xpyr	0.042	0.013	0.018		0.037		0.050		0.035		0.056		0.057		0.013
Xalm	0.630	0.450	0.476		0.573		0.487		0.447		0.584		0.532		0.222
XMg	0.062	0.029	0.037		0.060		0.093		0.072		0.087		0.097		0.054
Chlorite ^b	Metapelite						Calc.						Metabasite		
	29290			490°C/ 1.15 GPa			510°C/ 1.25 GPa			550°C/ 0.6 GPa			06CH02	29310	07CH06
Si	5.960	5.960	5.960		5.800		5.800		5.702		5.670		5.231		5.960
Al _t	2.040	2.040	2.040		2.200		2.200		2.298		2.330		2.769		2.040
Sum	8.000	8.000	8.000		8.000		8.000		8.000		8.000		8.000		8.000
Alo	2.457	2.080	2.080		2.200		2.200		2.502		2.216		2.584		2.330
Ti	0.012								0.020		0.002		0.003		0.008
Mn	0.069	0.100	0.100		0.100		0.100		0.173		0.305		0.048		0.039
Fe	3.903	4.700	4.720		4.160		4.160		4.779		5.719		5.515		2.937
Mg	5.638	5.120	5.100		5.540		5.364		4.364		3.750		3.930		6.753
Sum	12.079	12.000	12.000		12.000		12.000		11.838		11.993		12.084		12.067
OH	16.000	16.000	16.000		16.000		16.000		16.000		16.000		16.000		16.000
XMg	0.591	0.521	0.519		0.571		0.477		0.396		0.416		0.416		0.697
Epidote ^c	Metapelite						Calc.						Metabasite		
	29290			490°C/ 1.15 GPa			510°C/ 1.25 GPa		500°C/ 0.6 Gpa		500°C/ 1.10 Gpa		07CH06	530°C/ 1.25 Gpa	07CH06
Si	3.000	3.000	3.000		3.000		3.000		3.000		3.000		3.000		3.000
Al	2.342	2.400	2.480		2.440		2.493		2.600		2.400		2.616		2.320
Ti	0.018						0.006						0.009		0.003
Mg	0.007						0.002						0.001		0.003
Mn	0.021						0.029						0.025		0.125
Fe	0.660	0.520	0.560		0.546		0.800		0.580		0.628		0.680		0.929
Sum	3.048	3.000	3.000		3.075		3.000		3.000		3.279		3.000		3.228
Ca	1.995	2.000	2.000		2.000		1.973		2.000		2.100		2.000		1.853
Na	0.004						0.004				0.000		0.000		0.000
OH	1.000	1.000	1.000		1.000		1.000		1.000		1.000		1.000		1.000

Table 2 continued

Epidote ^c Stage	Metapelite 29290 II	Calc. 490°C/ 1.15 GPa		Calc. 510°C/ 1.25 GPa		Metabasite 07CH06 I.III		Calc. 530°C/ 1.10 GPa		07CH06 III		Calc. 550°C/ 0.6 Gpa		29310 I.III		29310 III	
		White mica ^d Stage Generation	29290 I Core	490°C/ 1.15 GPa	Calc. 510°C/ 1.25 GPa	II Core	Calc. 510°C/ 1.25 GPa	III Rim	Calc. 550°C/ 0.6 GPa	I.III	06CH12 I.II Core	06CH12 IV Sericite	06CH02 I.II Core	06CH02 III Rim	06CH02 IV Sericite	06CH02 IV Sericite	
Si	6.657	6.720	6.604	6.720	6.272	6.260	6.733	6.096	6.688	6.454	6.109						
Alt	1.344	1.280	1.396	1.280	1.728	1.740	1.267	1.904	1.313	1.546	1.891						
Sum	8.000	8.000	8.000	8.000	8.000	8.000	8.000	8.000	8.000	8.000	8.000						
Alo	2.894	3.280	3.012	3.280	3.361	3.760	3.111	2.799	3.060	3.513	3.766						
Ti	0.026	0.027	0.027	0.027	0.046	0.046	0.025	0.008	0.024	0.000	0.002						
Fe ³⁺	0.191	0.124	0.124	0.124	0.063	0.063	0.000	0.881	0.000	0.000	0.000						
Fe ²⁺	0.315	0.320	0.303	0.320	0.268	0.100	0.479	0.000	0.367	0.265	0.177						
Mn	0.002	0.000	0.000	0.000	0.000	0.004	0.004	0.001	0.003	0.005	0.005						
Mg	0.673	0.400	0.635	0.400	0.362	0.140	0.434	0.758	0.648	0.234	0.109						
Sum	4.100	4.000	4.100	4.100	4.100	4.000	4.053	4.100	4.102	4.016	4.060						
Ba	0.006	0.007	0.007	0.012	0.012	0.008	0.005	0.005	0.009	0.010	0.013						
Ca	0.000	0.000	0.000	0.000	0.000	0.001	0.002	0.014	0.171	0.027							
Na	0.094	0.160	0.104	0.160	0.131	0.160	0.118	0.102	0.112	0.188	0.016						
K	1.786	1.840	1.828	1.840	1.773	1.840	1.669	1.789	1.727	1.599	1.849						
Sum	1.887	2.000	1.940	2.000	1.916	2.000	1.795	1.899	1.862	1.967	1.905						
OH	4.000	4.000	4.000	4.000	4.000	4.000	4.000	4.000	4.000	4.000	4.000						
O'	19.945	20.000	19.973	20.000	19.965	20.000	19.902	19.949	19.943	20.074	19.973						
Paragonite	0.050	0.054	0.054	0.054	0.068	0.066	0.054	0.060	0.054	0.060	0.008						
Xtiroct.mica	0.050	0.050	0.050	0.050	0.050	0.050	0.026	0.050	0.051	0.008	0.030						
Xmuscovite	0.504	0.543	0.543	0.543	0.695	0.695	0.519	0.616	0.508	0.486	0.863						
XMgAlcelad.	0.226	0.207	0.207	0.207	0.082	0.082	0.176	0.096	0.227	0.149	0.029						
XFeAlcelad.	0.106	0.099	0.099	0.099	0.061	0.061	0.195	0.000	0.129	0.170	0.047						
XRest	0.064	0.048	0.048	0.048	0.045	0.045	0.017	0.228	0.025	0.092	0.023						
Plagioclase ^e		Metapelite		Calc.		Metabasite		Calc.		Metabasite		Metabasite		Metabasite		Metabasite	
Stage	29290	550°C/ 0.6 GPa	29310 III	06CH02 III	06CH13 III	29310 I.II	29310 III	06CH12 I.II Core	07CH06 III	06CH02 I.II Core	07CH06 III	06CH02 I.II Core	07CH06 III	06CH02 I.II Core	07CH06 III	06CH02 I.II Core	07CH06 III
Si	2.713	2.600	2.501	2.661	2.985	2.631	2.950									2.720	
Alt	0.287	0.400	0.499	0.339	0.015	0.369	0.050									0.280	
Sum	3.000	3.000	3.000	3.000	3.000	3.000	3.000									3.000	
Alo	0.992	1.000	0.986	0.977	0.984	0.903	0.986									1.000	

Table 2 continued

Stage	Plagioclase ^e	Metapelite			Calc.			Metabasite			550°C/ 0.6 GPa	550°C/ 0.6 GPa
		29290 III	550°C/ 0.6 GPa	06CH02 III	06CH13 III	29310 I,II	29310 III	07CH06 II-III	07CH06 II-III	06CH13 I		
Fe	0.014			0.007	0.002	0.002	0.141			0.006		
Mg	0.000			0.002	0.000	0.002	0.101			0.001		
Mn	0.001			0.002	0.000	0.000	0.008			0.000		
Sum	1.008			0.997	0.979	0.988	1.154			0.993		
Ca	0.286	0.400	0.463	0.354	0.005	0.005	0.224			0.010	0.280	
Na	0.700	0.600	0.000	0.000	1.040	1.040	0.627			0.000	0.720	
K	0.005		0.588	0.692	0.004	0.004	0.064			1.054		
Sum	0.991	1.000	1.056	1.050	1.050	1.050	0.917			0.004	1.000	
O'	8.000		8.000	8.000	8.000	8.000	8.000			1.069		
XAlbite	70.626	60.000	55.686	65.917	99.085	68.376	98.673			72.000		
XAnorthite	28.868	40.000	43.853	33.708	0.512	0.512	24.424			8.000	28.000	
XOrthoclase	0.505	0.000	0.419	0.375	0.403	0.403	6.927			0.946	0.000	
Amphibole ^f	07CH06 Incl. in gt	07CH06 Core	Calc. 500°C 1.1 GPa	07CH06 II Rim	Calc. 550°C 0.6 GPa	07CH06 III o. rim	Calc. 550°C 0.6 GPa	29310 I Core	29310 II Core	29310 III Rim	06CH13 I Core	06CH13 II Rim
Si	7.763	6.729	7.520	6.903	5.891	7.120	7.2549	6.820	6.360	6.925	6.481	
Al ^{IV}	0.211	1.271	0.480	1.097	2.109	0.880	0.745	1.180	1.640	1.075	1.519	
Sum	7.974	8.000	8.000	8.000	8.000	8.000	8.000	8.000	8.000	8.000	8.000	
Al ^{VI}	0.000	0.408	1.300	0.385	0.962	0.720	0.089	0.404	0.536	0.475	0.786	
Ti	0.003	0.039		0.032	0.026		0.014	0.029	0.037	0.024	0.038	
Mn	0.073	0.033		0.089	0.038		0.101	0.073	0.133	0.037	0.009	
F _{Fe} ³⁺	0.489	0.734		0.755	0.843		1.133	1.054	1.258	0.704	0.315	
F _{Fe} ²⁺	1.626	1.657	2.080	1.682	1.822	2.268	0.924	1.245	1.235	0.934	1.471	
Mg	2.834	2.130	1.620	2.059	1.309	2.012	2.740	2.195	1.801	2.827	2.382	
Sum	13.000	13.000	13.000	13.000	13.000	13.000	13.000	13.000	13.000	13.000	13.000	
Ca	1.854	1.851	1.120	1.807	1.853	2.000	1.611	1.596	1.589	1.657	1.852	
Ba	0.004	0.001		0.001	0.000		0.000	0.000	0.000	0.000	0.001	
Na	0.041	0.287	0.960	0.243	0.433	0.160	0.252	0.431	0.513	0.514	0.576	
K	0.010	0.061		0.036	0.114		0.023	0.041	0.081	0.023	0.061	
Sum	1.909	2.200	2.080	2.086	2.400	2.160	1.886	2.068	2.182	2.193	2.490	
OH	2.000	2.000	2.000	2.000	2.000	2.000	2.000	2.000	2.000	2.000	2.000	
Xtremolite	0.927	0.926		0.903	0.926		0.805	0.798	0.794	0.828	0.296	
Xglaucoph.	0.000	0.027		0.033	0.039		0.014	0.056	0.062	0.069	0.053	
Xriebeckite	0.073	0.048		0.064	0.034		0.181	0.146	0.144	0.103	0.021	

Table 2 continued

	29290 I	Calc. 490°C/ Core	29290 II	Calc. 510°C/ Rim	29290 III Fiss.	Calc. 550°C/ 0.6 Gpa	06CH12	06CH02 I	06CH02 II	06CH02 III
Si	5.269	5.960	5.384	5.960	5.378	5.600	5.549	5.286	5.465	5.543
Alt	2.731	2.040	2.616	2.040	2.622	2.400	2.451	2.714	2.535	2.457
Sum	8.000	8.000	8.000	8.000	8.000	8.000	8.000	8.000	8.000	8.000
Alo	0.521	0.040	0.615	0.040	0.766	0.400	0.887	0.668	0.573	0.571
Ti	0.194		0.193		0.172		0.232	0.142	0.162	0.170
Fe	2.467	2.840	2.401	2.680	2.305	2.520	2.243	2.701	2.585	2.363
Mg	2.740	3.060	2.724	3.260	2.534	3.020	2.253	2.277	2.458	2.635
Mn	0.023	0.060	0.026	0.060	0.023	0.060	0.022	0.082	0.105	0.110
Sum	5.944	6.000	5.959	6.000	5.800	6.000	5.637	5.870	5.883	5.849
Ca	0.099		0.058		0.000		0.006	0.002	0.006	0.008
Ba	0.007		0.006		0.008		0.004	0.012	0.011	0.016
Na	0.035		0.038		0.033		0.057	0.044	0.060	0.043
K	1.858	2.000	1.831	2.000	1.865	2.000	1.750	1.950	1.776	1.756
Sum	1.918		1.933		1.906	2.000	1.817	2.008	1.854	1.823
OH	4.000		4.000		4.000		4.000	4.000	4.000	4.000
XMg	0.526	0.519	0.532	0.532	0.524	0.545	0.501	0.457	0.487	0.527

Mineral compositions were obtained using a CAMECA SX 100 electron microprobe at Universität Stuttgart, Germany. Operating conditions were an acceleration voltage of 15 kV, a beam current of 15 nA, 20 s counting time per element and a defocused beam of 8 µm to avoid loss of alkalies in mica and amphibole. We used natural minerals, glasses and pure oxides as standards. The PAP correction procedure was used for matrix correction

^a Cations based on 48 negative charges including 10 cations in the tetrahedral and octahedral site to calculate Fe^{3+} ; o. rim = outer rim; calc. = calculated

^b Cations based on 56 negative charges; H_2O calculated on the basis of OH = 16

^c Proportions of cations are based on normalization of Si to three cations

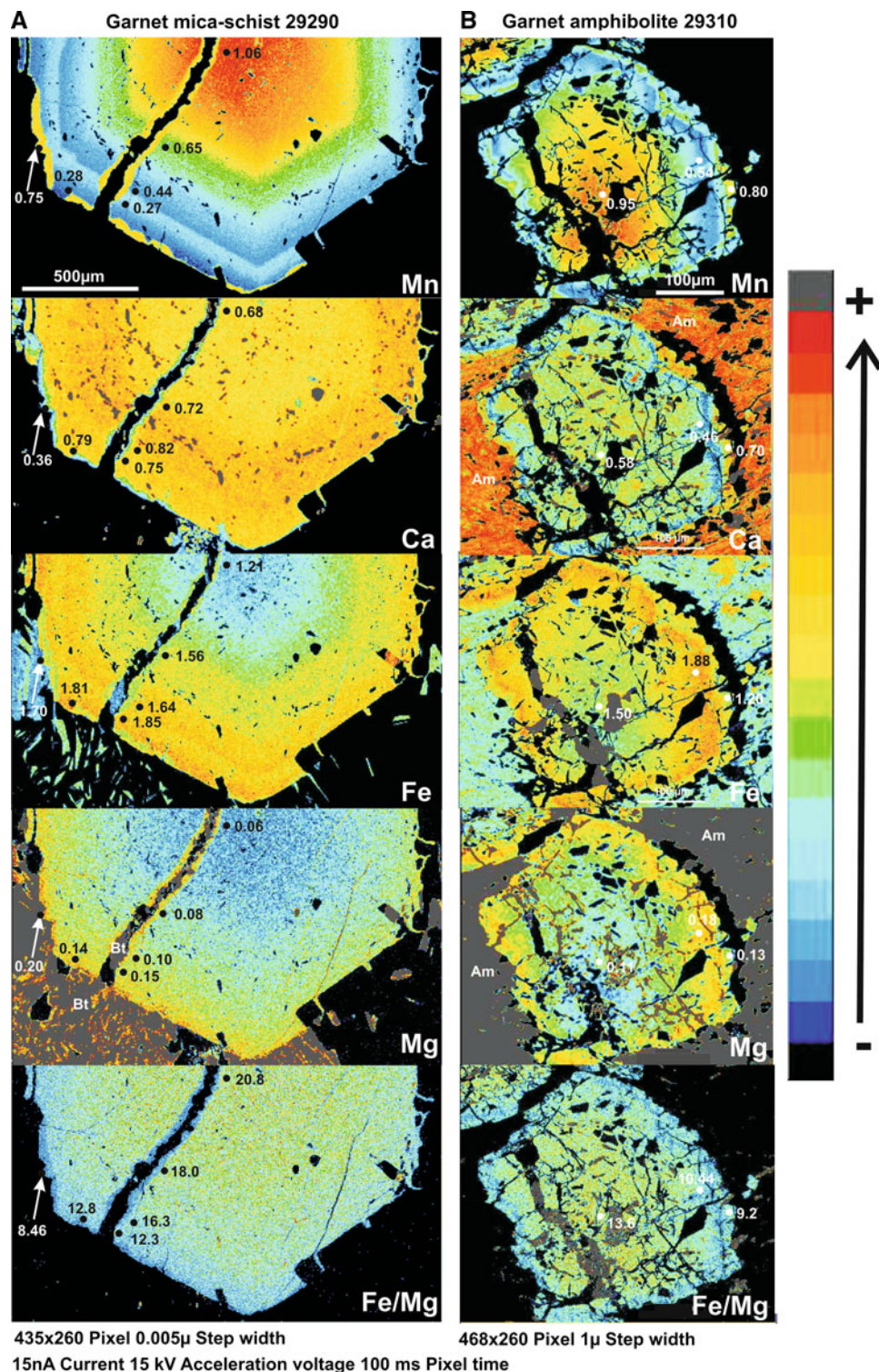
^d The proportion of cations is based on 42 negative charges neglecting the interlayer cations; the sum of octahedrally coordinated cations is set at 4.1 to allow for an estimation of Fe^{3+}

^e Normalization on the basis of 16 negative charges

^f Proportion of cations is based on the sum of cations = 13; except for Ca, Na and K for estimation of Fe^{3+} and on 46 negative charges; incl. = inclusion

^g Normalization on the basis of 22 negative charges; Fiss. = fissure

Fig. 2 Maps of X-ray intensity distribution of Mn, Ca, Fe, Mg and Fe/Mg in garnet from metapelite 29290 (**a**) and metabasite 29310 (**b**). Relative intensities increase from blue to red. Atomic proportions pfu of respective elements are given for each zone



phylllosilicate- and quartz-rich banding of up to 3 mm thickness. White mica, chlorite (0.1–0.5 mm) and biotite (0.2–0.5 mm) are strongly oriented parallel to the banding. Biotite also grew late as crosscutting grains. Some bands include crenulation of the phylllosilicates with recrystallized fold hinges. Ilmenite with rutile inclusions or rare

magnetite are the opaque minerals. Graphite, zircon and tourmaline are frequent accessories, whereas epidote is rare. Quartz, plagioclase and occasional potassie feldspar (0.1–0.5 mm) recrystallized as polygonal aggregates between the phylllosilicate bands. In most rocks, garnet grew as 1- to 5-mm-sized euhedral porphyroblasts

containing abundant titanite and quartz inclusions particularly in the core, where they are partly aligned parallel to a former crenulation foliation. Further inclusions of rutile, ilmenite, epidote, albite and chlorite are observed. Garnet overgrew a polygonal quartz fabric of similar size as that of the matrix only in its outer zones. Garnet rims are partly corroded by biotite that also grew within fissures cross-cutting the garnet crystals (Fig. 2a). Porphyroblasts of albite of 1–5 mm grew across the phyllosilicate bands containing abundant inclusions of apatite, chlorite, quartz, titanite, phengite and epidote. Rims around albite with sharp boundaries are composed of slightly altered plagioclase.

During late-stage alteration in most rocks, fine-grained aggregates of sericitic white mica and chlorite (0.01–0.05 mm) replaced large crystals of white mica, chlorite or biotite along the foliation planes as well as particularly garnet partly or completely. Pseudomorphs after garnet are by far more frequent than fresh garnet in the sampling area. Also matrix quartz can be corroded.

Garnet (andradite_{0.00–0.05}, grossular_{0.07–0.35}, spessartite_{0.13–0.50}, pyrope_{0.02–0.07}, almandine_{0.30–0.63}) shows a

growth zoning pattern (Fig. 2a; see also Massonne and Calderón 2008). From core to rim, Mn, Fe³⁺ and X_{Fe} decrease, whereas Fe²⁺ and Mg increase. Additionally, Mn and Fe show oscillatory zoning in the rim that is correlated with each other. At the outer rim and within fissures through the garnet, patch-like discordant garnet overgrew older garnet showing a strong increase in Mn and Mg and a decrease in Ca and Fe. It should be noted that particularly X_{Fe} = Fe²⁺/(Fe²⁺ + Mg) shows a continuous decrease, thus suggesting a steady temperature increase during garnet growth.

Coarse-grained *white mica* is phengite (Si 3.30–3.36 apfu) in the core and displays lower Si-contents at narrow rims (3.13–3.28 apfu; see also Massonne and Calderón 2008), whereas serizitic *white mica* is mainly muscovite (Si 3.02–3.25 apfu; Fig. 3a). Contents of Na (0.02–0.13) and X_{Mg} (0.1–0.7) vary widely but do not seem to be significantly distinct between generations. Compositions plot close to the ideal Tschermark's substitution line except for some sericitic grains due to substitution of some Al by Fe³⁺ (Fig. 3a).

Biotite shows little compositional variation without clear zoning within and among samples (X_{Mg} 0.44–0.55; Ti 0.16–0.39 apfu, Na 0.03–0.09 apfu) in contrast to chlorite (Si 4.98–6.67 apfu, X_{Mg} 0.39–0.63, Mn 0.02–0.21 apfu). Rare epidote in sample 29290 shows a variation in Fe³⁺ content at 0.66–0.98 apfu with no difference between matrix epidote and inclusions in garnet. Plagioclase is usually albite, but at discordant rims variable compositions were observed in different rocks (An₂₉, An_{41–44}).

Garnet–amphibolite

The predominant assemblage in the intercalated metabasite lenses is Ca – amphibole – garnet – epidote – chlorite – quartz – plagioclase – ilmenite – titanite ± magnetite (Table 1). Hypidioblastic amphibole (0.5–2 mm) is either oriented parallel to the penetrative foliation or unoriented. Cores are rich in quartz inclusions. Epidote (0.1–0.5 mm) and titanite aggregates are aligned parallel to the foliation. Hypidiomorphic porphyroblasts of garnet (1–5 mm) contain inclusions of ilmenite, titanite, epidote, chlorite and amphibole. Garnet rims, which are frequently corroded by chlorite, can contain large quartz inclusions with polygonal fabric. Matrix quartz forms polygonal aggregates partly with secondary recrystallization. Albite mostly grew as inclusion-rich porphyroblasts occasionally showing overgrowth of strongly sericitized plagioclase rims with sharp boundaries. K-feldspar may occur rarely. Most chlorite replaces a late retrograde phase replacing garnet and amphibole at its edges or along crosscutting fissures and is commonly intergrown with magnetite and/or ilmenite.

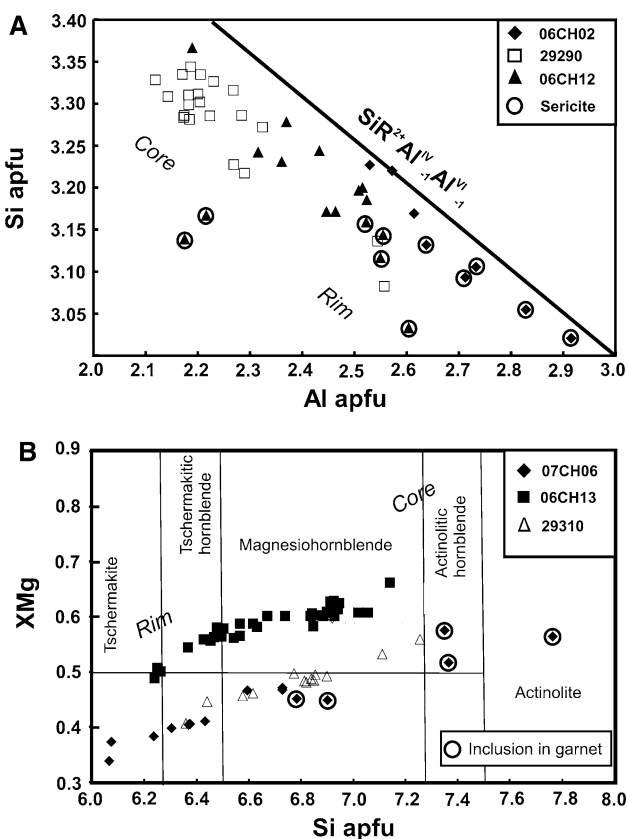
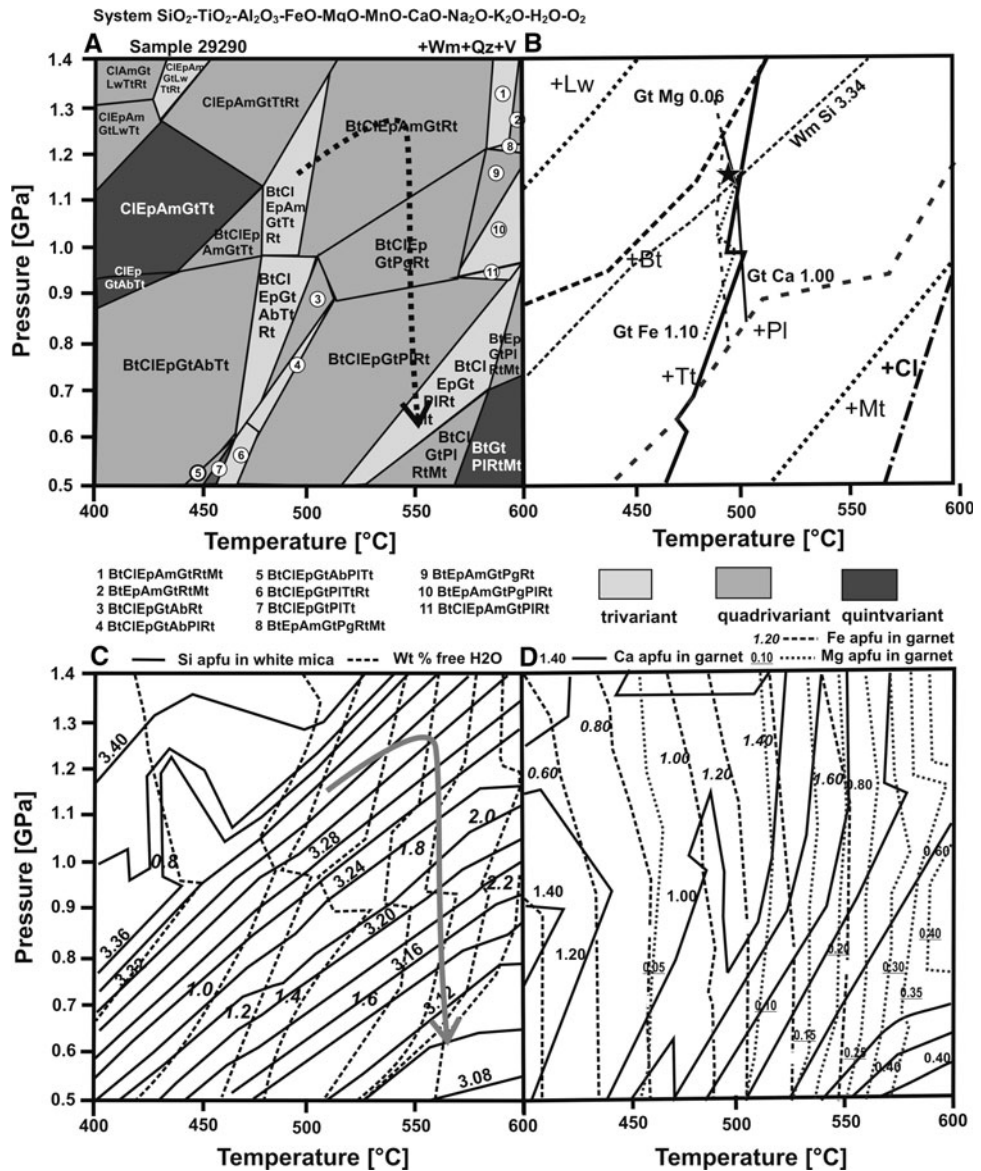


Fig. 3 **a** Si–Al variation diagram of white mica within the studied metapelitic samples **b** X_{Mg}–Si variation diagram of amphibole in the studied metabasite samples

Fig. 4 **a** P-T pseudosection calculated for metapelite 29290 (whole-rock analysis in Table 3) with the position of the PT path during growth of garnet; **b** stability fields of minerals as well as selected composition isopleths of garnet and white mica intersecting at the PT conditions during initiation of garnet growth (star); **c** isopleths of Si in white mica and wt% of free water; the inserted PT path indicates substantial water release after decompression; **d** isopleths for Ca, Fe and Mg in garnet



Biotite occurs in some K-rich amphibolite as well as occasional calcite.

Ca-amphibole is strongly zoned being actinolitic hornblende and magnesiohornblende in the core and tschermakitic hornblende and tschermakite at the rim (Fig. 3b; Si 7.3–5.9 apfu). This trend is correlated with decreasing X_{Mg} (0.35–0.66). Calculated contents of Fe^{3+} are variable (0.16–1.73 apfu) as those of $(\text{Na} + \text{K})_A$ (0.00–0.77 apfu) and $(\text{Na} + \text{K})_B$ (0.07–0.62 apfu), whereas Ti (0.01–0.08 apfu), Mn (0.01–0.13 apfu) and K (0.02–0.20 apfu) are present as traces only. Actinolite, actinolitic hornblende and magnesiohornblende occur as inclusions in garnet.

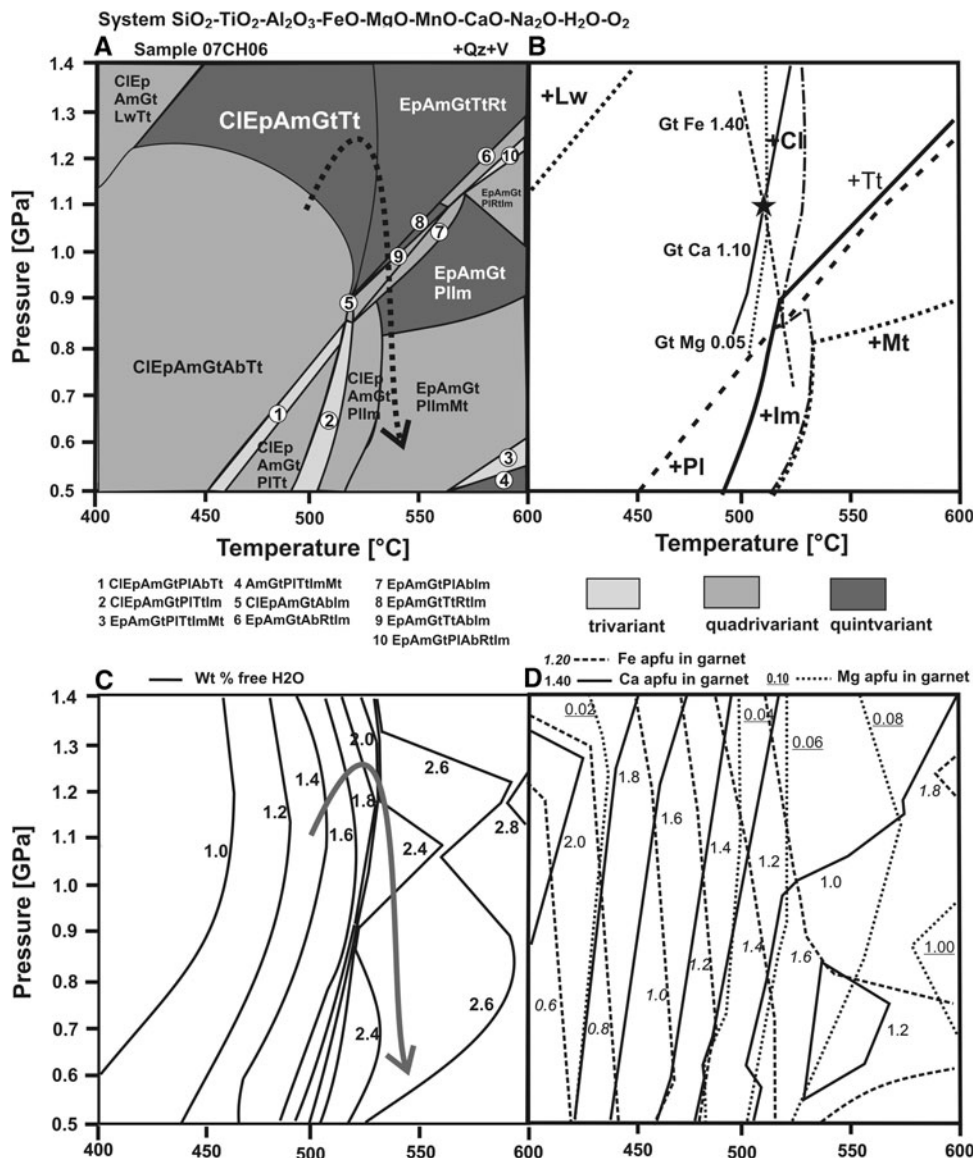
The growth zoning pattern of *garnet* (andradite $_{0.00-0.06}$, grossular $_{0.03-0.37}$, spessartite $_{0.04-0.58}$, pyrope $_{0.01-0.11}$, almandine $_{0.22-0.63}$) in the amphibolite is similar to that of

garnet in the metapelite except for Ca (Fig. 2b). From core to rim Mn, Ca and X_{Fe} decrease and Fe and Mg increase. At the outer rim overgrowth, patches of a discordant garnet show a strong increase in Mn and Ca and a decrease in Mg, Fe and X_{Fe} .

Chlorite shows intermediate Si-contents (5.06–5.97 apfu) and X_{Mg} (0.40–0.73) with little variation within samples and traces of Mn (0.01–0.31 apfu) and Ti (0.00–0.03 apfu). *Epidote* has Fe-contents of 0.63–0.87 apfu that are lower (0.55 apfu) in inclusions in garnet. *Plagioclase* is albite with rims containing 19–34 mol% anorthite component.

It should be noted that thin layers of garnet–amphibole quartzite with skeletal garnet growth are associated with metabasite lenses.

Fig. 5 **a** P-T pseudosection calculated for metabasite 07CH06 (whole-rock analysis in Table 3) with the position of the PT path during growth of garnet; **b** stability fields of minerals as well as selected composition isopleths of garnet intersecting at the PT conditions during initiation of garnet growth (star); **c** isopleths of wt% of free water; the inserted PT path indicates substantial water release during prograde garnet growth and decompression; **d** isopleths for Ca, Fe and Mg in garnet



Geothermobarometry

The predominant assemblages observed in the Guaruaraz Complex indicate albite–amphibolite facies conditions, i.e. the high pressure part of the amphibolite facies above $\sim 0.8\text{--}1.0$ GPa at $500^\circ\text{--}700^\circ\text{C}$, where only albite is the stable plagioclase up to at $\sim 1.5\text{--}1.7$ GPa. To explore the PT conditions, at which the predominant assemblages with garnet were formed at various stages, we have chosen two independent approaches: the calculation of (1) PT pseudosections and (2) mineral equilibria defined by intersection of multivariant reactions. For both methods, we selected different thermodynamic data sets to ensure independently derived PT data.

Pseudosections

Pseudosections for a metapelite (sample 29290; Fig. 4) and a metabasite (sample 07CH06; Fig. 5) were calculated with the PERPLE_X software package (Connolly 1990, 2005; used version of august 2006 downloaded from www.perple.ethz.ch). These samples were chosen from the petrographically investigated rocks, because no signs of metasomatism or veining were discernable and the dominating metamorphic assemblage was homogenously distributed at thin section scale. We used the thermodynamic data set of Holland and Powell (1998, updated 2002) for minerals and aqueous fluid and solid-solution models for white mica, epidote, garnet, plagioclase, amphibole,

Table 3 Whole-rock compositions

(Wt%)	Metapelite		Metabasite		Simplified compositions used for calculations of PT pseudosections	
	29290	07CH06	(Wt%)	29290	07CH06	
SiO ₂	65.8	48.1	SiO ₂	65.2	47.5	
TiO ₂	0.63	2.60	TiO ₂	0.63	2.57	
Al ₂ O ₃	15.5	12.8	Al ₂ O ₃	14.6	12.7	
FeO			FeO	5.64	15.17	
Fe ₂ O ₃	6.32	17.1	Fe ₂ O ₃			
CaO	1.04	10.4	CaO	1.72	10.3	
MgO	3.15	5.63	MgO	3.11	5.57	
MnO	0.33	0.25	MnO	0.33	0.25	
K ₂ O	4.17	0.38	K ₂ O	4.13		
Na ₂ O	0.61	2.02	Na ₂ O	0.60	2.00	
P ₂ O ₅	0.09	0.24	O ₂	0.04	0.10	
CO ₂	0.09	0.10				
H ₂ O	2.41	1.71	H ₂ O	3.96	3.94	
	100.1	101.3		100.0	100.0	

Analyses were obtained by a Philips PW 2400 X-ray fluorescence (XRF) spectrometer at Universität Stuttgart. Finely ground rock powder produced with a WC dish-and-puck mill was fused with Spectromelt® (ratio 1:9) to prepare glass discs

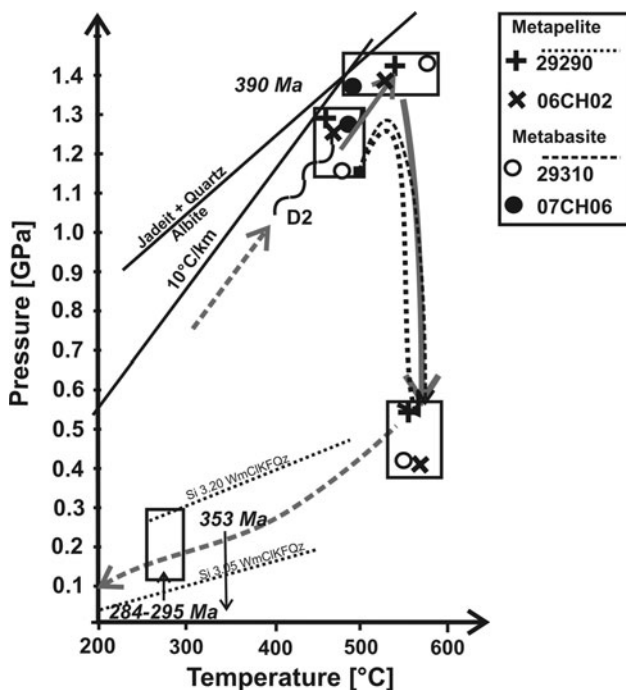


Fig. 6 Synoptic clockwise pressure–temperature–time–deformation path for the Guararaz Metamorphic Complex

chlorite and biotite reported by Holland and Powell (2003) and Powell and Holland (1999). Albite, K-feldspar, quartz, titanite, H₂O and paragonite were considered as pure

phases. For the calculation of the pseudosections, the major element compositions analysed by XRF were simplified to an 11-component system (SiO₂-TiO₂-Al₂O₃-FeO-MgO-MnO-CaO-Na₂O-K₂O-H₂O-O₂; K₂O = 0 for the metabasite and normalized to 100% (Table 3). Water contents were augmented to excess water conditions considered to have prevailed during peak PT conditions. Oxygen contents were estimated (0.04 resp. 0.1 wt%) to account for epidote and magnetite present in the samples. Calculated compositions of minerals provide good coincidence with measured ones (Table 2) except for amphibole, because the applied solid-solution model for amphibole can be taken as provisional only.

Calculated isopleths for the Ca, Fe and Mg contents in garnet are, in fact, strongly temperature dependent, but those for the inner garnet core cut at 1.15 GPa, 495°C and 1.10 GPa, 510°C for the metapelite and metabasite (Figs. 4, 5), respectively. For the metapelite, the isopleth of the maximum Si content for phengite (Si 3.35 apfu) also intersects the corresponding PT point. Thus, in both rock types, garnet started to grow in assemblage with chlorite, albite, titanite, epidote and amphibole (Figs. 4, 5) as calculated and in accordance with the observed inclusion assemblage. In the metapelite, additionally biotite, rutile and phengite were present at this stage. Most phases are observed as inclusions in garnet and albite. Only the presence of amphibole could not be proved in the studied metapelite samples but was observed as inclusion in albite by Massonne and Calderón (2008). Inclusions of actinolite in garnet of the amphibolite (Table 2) could point to early PT conditions lower than those derived here from the garnet core.

Further garnet growth in both rock types is due to higher temperatures according to the shift in compositional isopleths for garnet. The mineral assemblages are characterized by the disappearance of titanite and albite in the metapelite and metabasite, respectively. The temperature for this peak pressure stage can be constrained at about 530°C, because the rutile stability field is not reached in the metabasite. Under the assumption that white-mica compositions remained at >3.3 Si apfu as observed over most part of the large white-mica grains in the metapelite, pressure must have slightly increased to about 1.25 GPa.

For the latest stage of garnet growth (patchy overgrowths and fissure fillings), the corresponding mineral assemblages are garnet-biotite-chlorite-white mica-epidote-plagioclase-magnetite-rutile (metapelite) and the amphibole-garnet-epidote-plagioclase-ilmenite-magnetite (amphibolite) at considerably lower pressure, but higher temperature (<0.8 GPa; >550°C; Figs. 4a, 5a). Isopleths calculated for free water in the systems (Figs. 4c, 5c) show that during decompression, considerable fluid was released in the metapelite and the metabasite enhancing further growth and

Table 4 Lu–Hf isotopic compositions and derived mineral isochron ages

Sample	Fraction	Grain size [μ]	$^{176}\text{Lu}/^{177}\text{Hf}$	$\pm 2\sigma$	$^{176}\text{Hf}/^{177}\text{Hf}$	$\pm 2\sigma$	Lu (ppm)	Hf (ppm)	
29308	Garnet	200–300	0.56957	0.00342	0.286340	0.000007	1.985	0.495	Age = 391.7 ± 2.5 Ma
	Hornblende	200–300	0.02226	0.00013	0.282325	0.000006	0.104	0.662	Initial $^{176}\text{Hf}/^{177}\text{Hf} = 0.282161 \pm 5$
	Hornblende	100–200	0.01704	0.00010	0.282289	0.000011	0.081	0.672	MSWD = 0.88
	Whole rock		0.06229	0.00037	0.282611	0.000012	0.390	0.890	
07CH06	Hornblende	200–300	0.03760	0.00023	0.283069	0.000010	0.292	1.101	Age = 389.9 ± 2.4 Ma
	Hornblende	100–200	0.04080	0.00024	0.283100	0.000010	0.222	0.774	Initial $^{176}\text{Hf}/^{177}\text{Hf} = 0.282795 \pm 6$
	Garnet	100–300	1.39636	0.00838	0.292996	0.000010	0.850	0.087	MSWD = 1.60
	Whole rock		0.09585	0.00058	0.283491	0.000007	0.520	0.771	
29290	Garnet	200–300	0.68053	0.00408	0.287394	0.000007	6.468	1.350	Age = 388.3 ± 1.7 Ma
	Garnet	100–200	0.74319	0.00446	0.287827	0.000007	6.529	1.248	Initial $^{176}\text{Hf}/^{177}\text{Hf} = 0.282437 \pm 6$
	White Mica	200–300	0.01705	0.00010	0.282561	0.000006	0.085	0.709	MSWD = 0.49
	Whole rock		0.10259	0.00062	0.283183	0.000014	0.395	0.547	

For the Lu/Hf analyses about 100 mg of garnet, hornblende and mica (from sieve fractions of 100–200 and 200–300 μm) were handpicked under a binocular microscope. Mineral fractions were spiked and digested on a hotplate in closed Teflon vials to selectively dissolve the minerals excluding accessory phases like zircon and rutile (Lagos et al. 2007). Lu and Hf separation was achieved using ion-exchange columns (Münker et al. 2001), and the Hf fraction has been passed through an additional column to remove any remaining Lu and Yb (column A of Patchett and Tatsumoto 1980). Lu and Hf isotopic measurements were taken on a Finnigan Neptune MC-ICPMS at the Goethe-Universität Frankfurt, following the procedures described in Schmidt et al. (2008). Repeated measurements of a Lu-standard yielded a $^{176}\text{Lu}/^{175}\text{Lu} = 0.026556 \pm 31$ ($2\sigma \sim 0.12\%$, $n = 10$); the Hf standard JMC475 was reproduced with a $^{176}\text{Hf}/^{177}\text{Hf} = 0.282151 \pm 11$ ($2\sigma \sim 0.004\%$, $n = 11$). Isochrones were calculated using the ISOPLOT program (Ludwig 2007) with a $\lambda^{176}\text{Lu} = 1.867 \times 10^{-11}/\text{y}$ (Scherer et al. 2001; Söderlund et al. 2004)

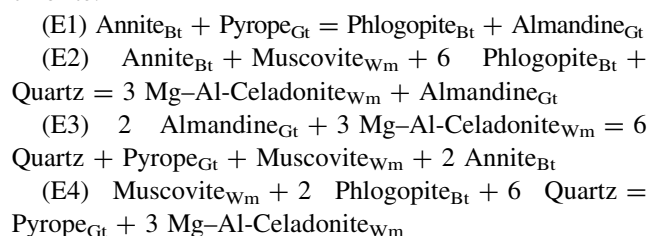
equilibration of the mineral phases at mid-crustal conditions as suggested by Massonne and Calderón (2008). During this decompression/heating path, albite porphyroblasts were growing in some rocks and the peristerite gap of plagioclase was overstepped during growth of their rims, when the midcrustal stage was reached with further temperature increase.

Multivariant reactions

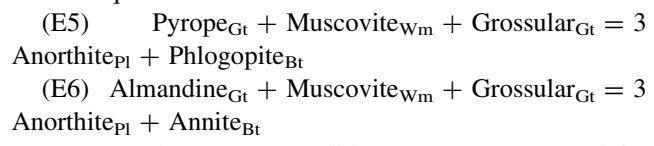
For calculating the PT position of multivariant reactions, we used the Ge0calc software of Brown et al. (1989) with the thermodynamic dataset of Berman (1988) augmented by compatible thermodynamic data of the following end-members: glaucophane (Evans 1990), clinochlore, Mg–Al-celadonite, Fe–Al-celadonite (Massonne 1995a), daphnite and muscovite (Massonne and Szpurka 1997). The used activity formulations for non-ideal solid solutions are as follows: chlorite and amphibole by Massonne (1995a, b), garnet by Berman (1990), feldspar by Fuhrman and Lindsley (1988), biotite by McMullin et al. (1991) and potassic white mica by Massonne (1995a, 1997). An ideal solid-solution model was chosen for epidote ($a_{\text{clinozoisite}} = 1 - X_{\text{pistazite}}$).

For the metapelitic samples 29290 and 29310, we used following multivariant equilibria combining core compositions of garnet, white mica and biotite and respective compositions of the cores (Table 2) to derive conditions

for the early stages according to the calculated PT pseudosection (Fig. 4a). However, the biotite composition does not vary considerably in contrast to that of chlorite.



To derive PT conditions for the late stage, we considered the composition of the Ca-rich plagioclase, the discordant garnet overgrowth and the outermost rim of white mica (Table 2) to calculate (E1) and the following multivariant equilibria:



For sample 29290 conditions are 1.31 GPa/463°C (early), 1.42 GPa/532°C (peak pressure) and 0.55 GPa/543°C (late). Comparable results were derived from sample 06CH02: 1.26 GPa/476°C, 1.45 GPa/563°C, 0.40 GPa/582°C (see also Table 1 and Fig. 6).

Similarly we calculated following multivariant equilibria for the three stages of garnet growth also in the metabasite samples 29310 and 07CH06 using core, rim and

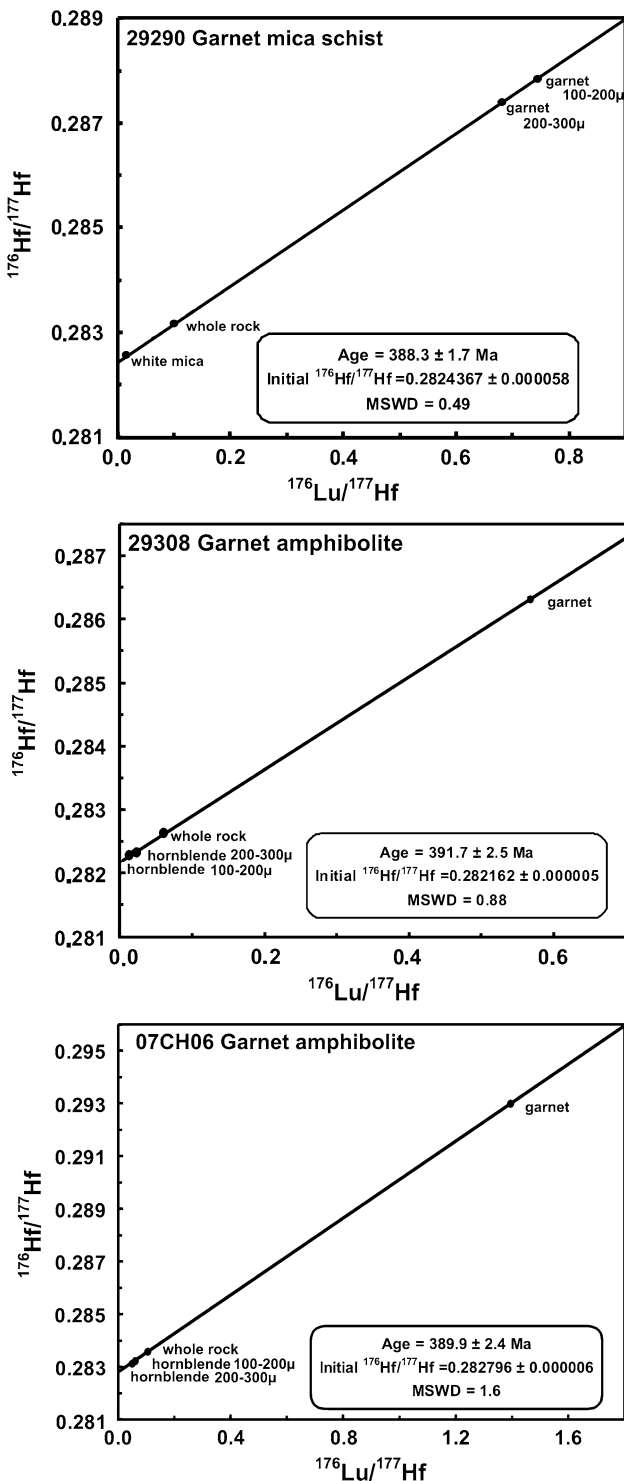
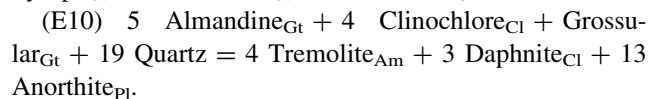
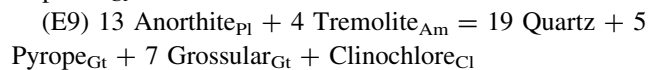
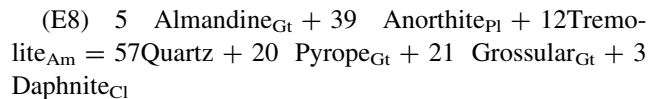
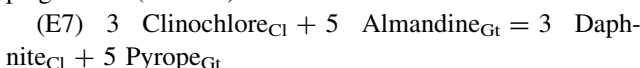


Fig. 7 Lu–Hf isochrones for metapelitic sample 29290 and metabasic samples 07CH06 and 29308

outer rim compositions of garnet, amphibole, chlorite and plagioclase (Table 2):



For sample 29310 1.13 GPa/495°C (early), 1.42 GPa/592°C (peak pressure), 0.41 GPa/555°C (late) result, for 07CH06 1.28 GPa/480°C and 1.36 GPa/495°C (see also Table 1 and Fig. 6). The resulting PT path during garnet growth is comparable for both major rock types (Fig. 6) and also coincides with that of Massonne and Calderón (2008).

A retrograde fluid infiltration is defined by the growth of sericitic white mica in the metapelitic and chlorite in all rock types. The very low grain size of both minerals suggests low crystallization temperatures ($\sim 250\text{--}350^\circ\text{C}$). The geobarometer reaction

(E11) 5 Al-celadonite_{Wm} + Muscovite_{Wm} = 6 K-feldspar + Clinochlore_{Cl} + 2 Quartz + 2 H₂O was calculated for the K-feldspar-bearing samples 06CH02 and 06CH12 considering the compositional range of sericite (Si 3.2 and 3.05 apfu). The calculation results indicate the approximate PT field of the hydrous fluid infiltration at $\sim 250\text{--}350^\circ\text{C}$ and 0.1–0.3 GPa (Fig. 6). Pressures can be corroborated by the pressures of intrusions of Carboniferous post-collisional granitoids which caused wide contact aureoles including andalusite. Stability of andalusite with muscovite and quartz (sample 06CH24; Table 1) also occurs at 0.1–0.3 GPa.

Geochronology

The Lu–Hf system

Exact timing of the peak of the HP metamorphism is of key importance, because this age will also approximate the time of microplate collision. We have chosen the Lu–Hf system because of (1) its wide use for precise dating of garnet-bearing assemblages, (2) its presumed high closure temperature of $\geq 700^\circ\text{C}$ (Scherer et al. 2000) resulting in mineral crystallization ages at medium grade conditions, (3) a good link of ages to PT conditions and (4) a potentially good age correlation between metabasite and metapelitic. One metapelitic and two amphibolite samples were selected that showed no evidence of retrograde mineral growth. In these samples, no detrital zircon was detected that contains high inherited Hf contents to bias whole-rock isotopic composition.

Three four-point mineral isochrones for rocks of metapelitic and metabasic composition (Table 4; Fig. 7)

Table 5 Results of ${}^{40}\text{Ar}/{}^{39}\text{Ar}$ dating of single white-mica grains by stepwise heating with CO₂ laser

Sample ID	Step	Laser output (%)	Age	± 1 s	${}^{40}\text{Ar}^*/{}^{39}\text{Ar}_{\text{K}}$	± 1 s	${}^{40}\text{Ar}/{}^{39}\text{Ar}$	± 1 s	${}^{37}\text{Ar}/{}^{39}\text{Ar}$	± 1 s	${}^{36}\text{Ar}/{}^{39}\text{Ar} \times 10^3$	± 1 s	${}^{40}\text{Ar}^*$	${}^{39}\text{Ar}_{\text{ca}}/{}^{39}\text{Ar}_{\text{K}}$		
29290	1	1.6	105.46	21.31	29.224	6.079	115.653	3.229	0.317	0.065	292.655	21.018	25.261	0.208	1.856	
	2	1.8	240.97	13.19	69.369	4.047	91.584	1.897	0.105	0.040	75.249	12.623	75.736	0.376	5.594	
	3	2.2	318.65	3.80	93.779	1.160	99.920	0.871	0.064	0.007	20.830	2.720	93.848	1.700	9.215	
	4	2.4	344.62	2.26	102.177	0.613	104.693	0.524	0.101	0.008	8.593	1.124	97.587	3.164	5.833	
	5	2.6	338.11	1.90	100.063	0.468	102.108	0.435	0.483	0.006	7.291	0.626	97.951	6.735	1.218	
J:0002057	6	2.8	352.48	1.42	104.744	0.203	105.060	0.159	0.155	0.003	1.191	0.432	99.684	8.095	3.800	
	7	3.0	352.33	1.44	104.695	0.215	105.539	0.190	0.108	0.001	2.941	0.348	99.190	11.631	5.449	
	8	3.2	354.40	1.46	105.372	0.226	105.362	0.208	0.091	0.002	0.038	0.294	100.001	14.254	6.487	
	9	3.4	351.31	1.36	104.362	0.152	104.522	0.129	0.124	0.002	0.637	0.271	99.835	15.723	4.738	
Mica-schist	10	3.6	351.90	1.40	104.555	0.190	105.635	0.178	0.276	0.002	3.869	0.235	98.952	16.330	2.130	
	11	4.0	353.93	1.39	105.219	0.169	106.957	0.163	0.217	0.001	6.052	0.174	98.354	21.700	2.715	
	352.7	0.6	Plateau age; plateau steps are from 6 to 11					350.3	0.3	Total gas age						
06CH12	1	1.6	352.7					352.0	1.7	Normal isochron age from plateau steps	Initial ${}^{40}\text{Ar}/{}^{36}\text{Ar}$ ratio: 312 \pm 42					
	2	2.0	81.17	20.44	22.231	5.726	142.961	4.328	0.044	0.051	408.584	21.399	375 \pm 36	MSWD	1.84	
	3	2.4	150.42	4.68	42.005	1.351	80.514	0.721	0.070	0.016	130.358	4.377	52.168	1.920	2.12	
	4	2.8	216.81	2.65	61.690	0.761	73.171	0.483	0.063	0.008	38.894	2.144	84.304	4.062	9.359	
	5	3.2	274.06	1.54	79.255	0.360	85.624	0.250	0.026	0.003	21.570	0.933	92.560	8.815	23.062	
J:0002064	6	3.4	293.89	1.22	85.471	0.173	87.514	0.123	0.015	0.001	6.923	0.419	97.665	15.173	40.073	
	7	3.6	287.72	1.20	83.530	0.177	84.851	0.150	0.032	0.002	4.492	0.327	98.440	19.232	18.584	
	8	3.8	280.63	1.17	81.307	0.167	82.621	0.082	0.012	0.002	4.455	0.495	98.409	21.796	49.020	
Mica-schist					272.23	1.07	78.686	0.114	0.289	0.109	0.036	0.001	5.451	0.129	97.999	28.392
No plateau					274.9	0.3	Total gas age	274.9	0.3	Total gas age	Initial ${}^{40}\text{Ar}/{}^{36}\text{Ar}$ ratio: 312 \pm 42					
06CH03	1	1.6	17.23	44.28	5.613	17.234	63.070	1.011	1.111	111.091	194.946	4.618	8.890	1.218	0.529	
	2	1.8	51.61	28.74	16.971	51.609	29.265	0.461	0.730	73.012	41.967	2.285	57.949	1.855	0.805	
	3	2.2	121.34	8.89	40.686	121.342	54.580	0.355	0.225	22.540	47.148	0.572	74.527	6.015	2.609	
	4	2.4	241.24	6.17	83.668	241.240	91.396	0.277	0.146	14.648	26.257	0.253	91.532	9.263	4.015	
	5	2.5	290.77	5.43	102.273	290.767	105.840	0.301	0.122	12.233	12.164	0.509	96.619	11.111	4.808	
J:0001710	6	2.6	296.06	5.88	104.292	296.060	106.893	0.359	0.132	13.207	8.907	0.238	97.554	10.298	4.453	
	7	2.7	293.24	8.97	103.215	293.239	105.872	0.385	0.206	20.553	9.151	0.317	97.471	6.620	2.861	
	8	2.8	299.35	6.14	105.551	299.353	109.032	0.763	0.132	13.153	11.883	0.752	96.795	10.351	4.472	
Mica-schist	9	2.9	321.75	2.58	114.173	321.746	116.745	0.276	0.050	4.956	8.742	0.150	97.793	27.474	11.869	
	10	3.0	331.40	16.76	117.925	331.403	119.236	0.516	0.374	37.426	4.748	0.626	98.864	3.643	1.571	

Table 5 continued

Sample ID	Step	Laser output (%)	Age	± 1 s	$^{40}\text{Ar}^*/^{39}\text{Ar}_\text{K}$	± 1 s	$^{40}\text{Ar}/^{39}\text{Ar}$	± 1 s	$^{37}\text{Ar}/^{39}\text{Ar} \times 10^3$	± 1 s	$^{36}\text{Ar}/^{39}\text{Ar} \times 10^3$	± 1 s	$\%^{40}\text{Ar}^*$	$\%^{39}\text{Ar}_\text{K}$	$^{37}\text{Ar}_\text{Ca}/^{39}\text{Ar}_\text{K}$
11	3.8	326.47	6.63	116.006	326.471	118.068	0.245	0.147	14.654	7.096	0.328	98.240	9.311	4.014	
12	6.0	338.68	21.62	120.767	338.685	124.877	0.542	0.481	48.057	14.311	0.922	96.663	2.840	1.223	
		322.7	2.4	Plateau age: plateau steps are from 9 to 12											
		285.7	2.3	Total gas age											
		329.4	21.0	Normal isochron age from plateau steps											
		46.0	92.0	Inverse isochron age from plateau steps											
					Initial $^{40}\text{Ar}/^{36}\text{Ar}$ ratio:										
					Initial $^{40}\text{Ar}/^{36}\text{Ar}$ ratio:										

$^{40}\text{Ar}/^{39}\text{Ar}$ dating was performed in the $^{40}\text{Ar}/^{39}\text{Ar}$ geochronology laboratory at Universität Potsdam after neutron activation of large white-mica crystals (1 mm diameter) at the Geesthacht Neutron Facility (GeNf) of the GKSS in Geesthacht, Germany. Full details of the Ar/Ar analytical system of Potsdam and the method are given in Willner et al. (2009a) or Wiederkehr et al. (2009). Two irradiations were conducted for this study. The package was Cd-shielded and irradiated with fast neutrons with a flux of $1 \times 10^{12} \text{n/cm}^2/\text{s}$ for 97 h (for 06CH03) or 96 h (for 29290 and 06CH12). The Fish Canyon Tuff sandine (age 27.5 Ma; Uto et al. 1997; Ishizuka et al. 2002) was used as a flux monitor to obtain the J values. K_2SO_4 and CaF_2 crystals were also irradiated to correct interference of Ar isotopes produced by the reactions on K or Ca in the samples. The Ar isotopic analytical system used consists of (1) a New Wave Gantry Dual Wave laser ablation system with a 50 W CO_2 laser (wavelength 10.6 μm), (2) an ultra-high vacuum purification line with SAES getters and a cold trap held at the freezing point of ethanol and (3) a Micromass 5400 noble gas mass spectrometer adopted a pulse counting system with an electron multiplier. The unknown white-mica grain samples were heated by a defocused continuous CO_2 laser beam with sizes up to 1,500 μm and for up to 1 min. The extracted gas was purified with getters and a cold trap and then was introduced to the noble gas mass spectrometer. The Ar isotopic ratios of the sample gas were finally obtained after corrections of blank, mass discrimination by analysis of standard atmospheric argon, interference of the Ar isotopes derived from Ca and K and the decay of produced radiogenic ^{37}Ar and ^{39}Ar . The calculation of the ages and errors was performed according to Uto et al. (1997).

were determined by measuring the isotope ratios of two different minerals (garnet-hornblende or garnet-white mica), two grain size fractions of one mineral and the whole rock. The isochrones yield a very narrow age spectrum of almost identical ages at 388.3 ± 1.7 Ma ($\pm 2\sigma$) (metapelite 29290), 389.9 ± 2.4 Ma (metabasite 07CH06) and 391.7 ± 2.5 Ma (metabasite 29308) with an average of the three samples at 390.0 ± 2.2 Ma ($\pm 2\sigma$).

Temperature during garnet crystallization can be considered below or at the lowest level of the assumed closure temperature range for the Lu–Hf system at 550–800°C depending on cooling rate and grain size (Scherer et al. 2000; Anczkiewicz et al. 2007). Hence, the resulting ages are crystallization ages of the predominant garnet-bearing assemblage. Both major rock types of contrasting origin in the Guarapari Complex show identical ages. This means that both rock types were already juxtaposed against each other before the peak of HP metamorphism.

The $^{40}\text{Ar}/^{39}\text{Ar}$ system

We analysed single large phengite grains of ~1 mm size in three metapelite samples by the step heating method using $^{40}\text{Ar}/^{39}\text{Ar}$ laser ablation (Table 5; Fig. 8). Due to the low commonly accepted closure temperature of the $^{40}\text{K}-^{40}\text{Ar}$ system of ~350–420°C (McDougall and Harrison 1999 and references therein) with respect to the peak temperatures of the Guarapari Complex, we could expect cooling ages. However, the selected samples differ in the degree of late retrograde fluid infiltration and alteration indicated by the amount of sericite and fine-grained chlorite. Sample 29290 contains no sericite, but samples 06CH03 and 06CH12 contain considerable contents of this mineral.

The oldest $^{40}\text{Ar}/^{39}\text{Ar}$ plateau age of 352.7 ± 0.6 Ma in sample 29290, in which the plateau consists of 88% of total $^{39}\text{Ar}_\text{K}$ released (Fig. 8), is identical with the normal isochron age of 352.7 ± 1.7 Ma with an initial $^{40}\text{Ar}/^{36}\text{Ar}$ ratio of 312 ± 42 close to that of atmospheric Ar (295.5). Because this well-defined $^{40}\text{Ar}/^{39}\text{Ar}$ age is 40 Myrs younger than the Lu–Hf crystallization age of the white mica of 391.7 ± 2.5 Ma, it must be interpreted as a cooling age. In general, the presence of fluids and/or deformation are essential for diffusion to proceed at a specific stage (Villa 1998). In the present case, retrograde deformation was absent, but sufficient internally generated hydrous fluid should have been released during decompression to mid-crustal conditions (see Figs. 4c, 5c) to trigger Ar diffusion during cooling.

By contrast, the two further samples show consistently younger ages and more irregular Ar age spectra pointing to partial Ar loss: In sample 06CH03, the lower temperature steps show a broad increasing positive slope typical for an

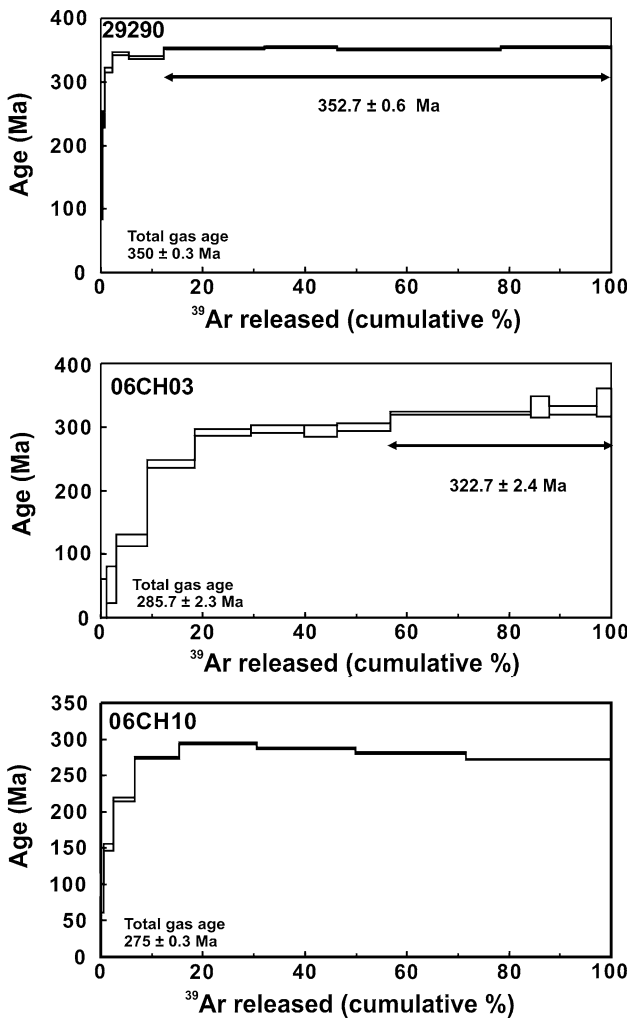


Fig. 8 ^{39}Ar release spectra for metapelitic samples 29290, 06CH03 and 06CH12

Ar loss curve. A plateau age of 322.7 ± 2.4 Ma may be derived only from the last steps with 43% of the $^{39}\text{Ar}_\text{K}$ total amount released (Fig. 8). However, it appears to be an apparent plateau without geological meaning, because it is considerably younger than the well-defined plateau age of

sample 29290 in spite of the same geological history of both samples. In sample 06CH12 (with most sericite and hence most alteration), the investigated large grain of white mica shows an Ar release spectrum without any plateau. We interpret both irregular spectra as due to a resetting of the Ar–Ar ages at temperatures lower than the closure temperature of the K–Ar system coupled to the late external fluid influx. It must be noted that in both samples with resetted Ar–Ar ages, the original chemical composition of Si-rich white mica is still preserved. Similar Ar-age resetting at low temperature has also been detected in rocks of accretionary prisms in South Chile by Ramírez-Sánchez et al. (2007) and Willner et al. (2009a).

However, although age resetting can be correlated with late fluid influx, it is difficult to envisage the mechanism of resetting. Considering the large grain size of white mica I and presumably low temperatures of the influx event ($\sim 250\text{--}350^\circ\text{C}$), it is difficult to explain resetting by diffusion. An in situ dissolution/precipitation process might be envisaged, but this should have influenced the original white-mica composition. Alternatively cleavage planes of white mica could have been pathways for a fluid causing resetting at low temperatures and shallow depths. Ar loosely bound in the mica interlayer position will have been removed by these fluids.

Zircon fission tracks

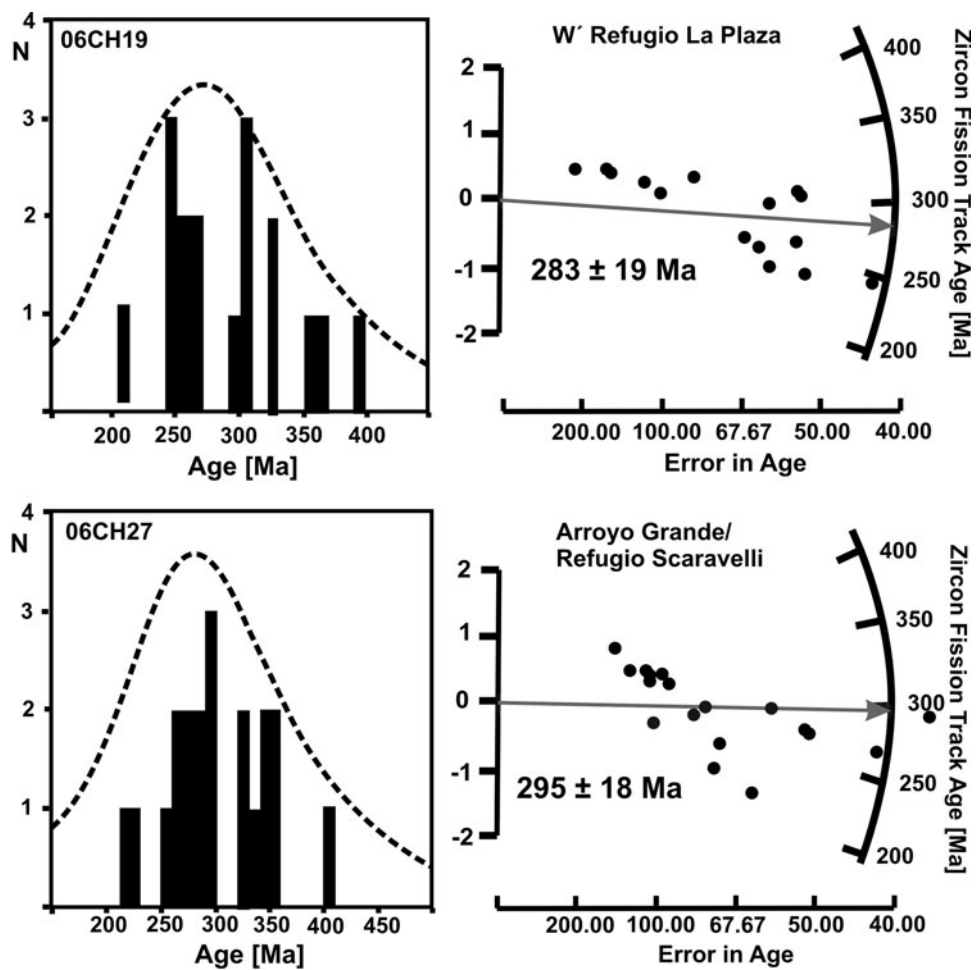
We selected two rocks for fission-track dating of zircon from different parts of the Guararaz Complex to get information about the latest detectable stage of exhumation. Sample 06CH19 is from a zone not overprinted by a late low-pressure/high-temperature metamorphism, whereas sample 06CH27, taken from the Arroyo Grande in the Portillo Area in the southern part of the Guararaz Complex, is characterized by growth of andalusite during a contact metamorphic overprint associated with granitoid intrusion. Resulting ages of 283.5 ± 18.8 (sample 06CH19) and 295.4 ± 17.8 (sample 06CH27) are identical within the 2σ error (Table 6; Fig. 9).

Table 6 Fission-track data for zircon from the metamorphic basement ($31^\circ\text{--}32^\circ\text{S}$)

Sample	<i>N</i>	Track density ($\times 10^6 \text{ tr cm}^{-2}$)			Age dispersion (P χ^2)	Central age (Ma) ($\pm 1\sigma$)
		Ps (Ns)	Pi (Ni)	Pd (Nd)		
06CH27	20	15.67 (4,039)	1.622 (418)	0.5140 (3,208)	<0.01% (99%)	295.4 ± 17.8
06CH19	16	17.25 (3,026)	1.870 (328)	0.5163 (3,222)	<0.01% (99%)	283.5 ± 18.8

Zircon crystals were separated, mounted, polished and etched according to Thomson and Ring (2006), analysed applying the external detector method and irradiated with Corning dosimeter glass CN5 at the Oregon State University Triga Reactor, Corvallis, USA. Central ages (Galbraith and Laslett 1993) quoted with 1σ errors were calculated using the Zeta-calibration approach of Hurford and Green (1983). The CN5 zeta calibration factor of 371.5 ± 14.0 (zircon) was obtained by repeated calibration against age standards according to Hurford (1990)

Fig. 9 Histogram and radial plot representation of zircon single grain FT age data for selected rocks of the study area



Fission tracks in zircon shorten or anneal with increased temperature and duration of heating. For pristine zircon grains, annealing over geologic time begins at $250 \pm 20^\circ\text{C}$, with total resetting occurring above $310 \pm 20^\circ\text{C}$ (Tagami et al. 1998), although these temperatures are lower in zircon with high accumulated radiation damage (Rahn et al. 2004). This translates into a closure temperature for fission tracks in zircon at moderate-to-fast cooling rates of $280 \pm 30^\circ\text{C}$, which correlates well with the brittle/ductile transition (Brix et al. 2002).

The age range by the two samples can be considered as a valid late cooling age below this temperature for the entire Guarapari Complex.

Discussion and geotectonic constraints

The prograde PT path and HP stages

Titanite and low Na actinolite enclosed in garnets of the metapelite and metabasite, respectively, are relics of the early prograde path at low PT. Possible PT conditions of a

pre-HP stage at $\sim 0.8 \text{ GPa}, 500^\circ\text{C}$ were proposed by Massonne and Calderón (2008). Penetrative deformation D₂ occurred during the prograde path only up to the time of early garnet growth (folded inclusion trails). This event was followed by static recrystallization within all rock types. The resulting polygonal fabric is already overgrown by garnet rims. Hence, D₂ can be correlated with burial.

Peak pressure conditions evolved around a low metamorphic gradient of $\sim 10\text{--}12^\circ\text{C/km}$, when main garnet growth occurred from mean PT conditions of $1.22 \pm 0.05 \text{ GPa}, 470^\circ \pm 30^\circ\text{C}$ to $1.40 \pm 0.05 \text{ GPa}, 530^\circ \pm 50^\circ\text{C}$. Continent-derived metasediments and the metabasite of oceanic origin were already mixed at that time and also reveal the same exhumation history as proved by the coinciding peak PT conditions and ages of the pressure peak.

The Lu–Hf isochrones show that garnet was in equilibrium with hornblende or white mica resulting in identical crystallization ages with a mean of $390.0 \pm 2.2 \text{ Ma}$ (Fig. 7). Many studies of REE distributions in garnet have shown that Lu is generally concentrated in the core of garnet resulting in a bell-shaped zoning pattern particularly

at medium grade (e.g. Skora et al. 2006; Anczkiewicz et al. 2007; Schmidt et al. 2008; Konrad-Schmolke et al. 2008). Hence, the resulting ages—although they represent a mixture of ages of the three growth stages—are more weighted towards those of the garnet core. On the other hand, the low volume of late garnet grown at intermediate pressure suggests little or no influence on the age of the bulk volume of garnet. Hence, dated initial garnet growth can be correlated with the burial process caused by the collision of Chilenia with Gondwana.

Peak temperature stage

It was shown that during the early decompression event, considerable amounts of water were released (Figs. 4c, 5c). Thus, it is conceivable that reactions and equilibration continued during the decompression path. Albite porphyroblast growth is related to this stage. Rim compositions of albite, amphibole, white mica, occasional small rims of discordant garnet overgrowth as well as biotite filling fissures in garnet define a third stage of equilibration at midcrustal conditions around 0.49 ± 0.08 GPa, $560^\circ \pm 30^\circ\text{C}$, whereas Roviños et al. (1997) and Massonne and Calderón (2008) determined 0.8 GPa at these temperatures. In any case, a heating during decompression is independent of the applied geothermobarometric method.

Retrogression stages

The calculated formation of hydrous fluids during decompression should have aided diffusion of the $^{40}\text{Ar}/^{39}\text{Ar}$ system in white mica (Villa 1998). We derived one well-defined $^{40}\text{Ar}/^{39}\text{Ar}$ plateau age of 352.7 ± 0.6 Ma of white mica that contrasts its Lu–Hf crystallization age of 388.3 ± 1.7 Ma (Fig. 7a) and is interpreted as age of cooling under $\sim 350\text{--}420^\circ\text{C}$. From the geometry of the PT path (Fig. 6) and the conditions of the retrogression stage, a pressure of $\sim 0.2\text{--}0.3$ GPa is assumed for this temperature range. This pressure is equivalent to a depth of 7–11 km (on the basis of a mean crustal density of 2.8 g/cm^3). If we take a depth of 46–50 km for the peak of metamorphism into account, a minimum average exhumation rate of 0.9–1.2 mm/a results for the period 390–353 Ma. Exhumation rates during the heating/decompression path can still have been considerably higher. Nevertheless, the derived average rate contrasts significantly lower rates known from the coastal accretionary systems of Chile around 0.5 mm/a consistent with mean worldwide erosion rates and erosion as prime exhumation factor (Glodny et al. 2005; Willner et al. 2005). The higher rate for the Guararaz Complex is more compatible with erosion of morphologically clearly exposed mountain ranges like the Alps or Himalaya.

After cooling to below $\sim 350^\circ$, a late pervasive influx of hydrous fluids caused the growth of sericite in most metapelites and considerable chloritization in both metapelite and metabasite at $\sim 250\text{--}350^\circ\text{C}$ and 0.1–0.3 GPa (Fig. 6). This event occurred in shallow crustal levels, where hydrothermal circulation is possible. It might have been a time-equivalent to the still ill-defined episode of post-collisional granite intrusions at 348 ± 35 to 337 ± 15 Ma (Caminos et al. 1979) in the Guararaz Complex and related to a high geotherm caused by intruding granitoids and/or an episode of extension.

This late stage of the retrograde PT evolution is related to a uniform exhumation level where the entire Guararaz Complex cooled under 280°C as dated by fission tracks in zircon at 284 ± 19 to 295 ± 18 Ma. This age marks the end of an early episode of granite intrusions, a pervasive shallow crustal hydrous fluid influx and a period of a considerable decrease in average exhumation rates to 0.1–0.05 mm/a during the period of 353–290 Ma when the Guararaz mountain range was already denuded. However, these exhumation rates must be seen as minimum rates, because a reburial of the basement within shallow crustal levels cannot be excluded due to the existence of unconformably overlying Upper Carboniferous sediments (El Plata Formation; Caminos 1979) on the basement. Considering the error, the FT-ages may still be Carboniferous (299–360 Ma; Ogg et al. 2008). Possible reburial within the uppermost crust during Carboniferous times can only have occurred at the basis of the local Carboniferous basin under a high geothermal gradient.

Geodynamic consequences

The derived PTtd history of the Guararaz Complex contrasts the well-known evolution of the late Palaeozoic coastal accretionary systems in central Chile (e.g. Willner 2005; Willner et al. 2005; Glodny et al. 2005; Richter et al. 2007) that developed after collision of Chilenia with Gondwana at its Pacific side. The following characteristics of the PTtd evolution in the Guararaz Complex can be considered as typical for a collisional setting between colliding continental crustal blocks (also outlined by Massonne and Calderón 2008):

1. In contrast to the coastal accretionary systems in Chile, there was no subduction of contemporaneous continental margin sediments, but rather neritic epicontinental sediments deposited in a basin outside its present position in Late Precambrian to Lower Cambrian times (Lopez and Gregori 2004; Lopez et al. 2009; Willner et al. 2008).
2. Peak pressure conditions occurred at 1.40 GPa, 530°C around a low metamorphic geotherm of $10\text{--}12^\circ\text{C/km}$

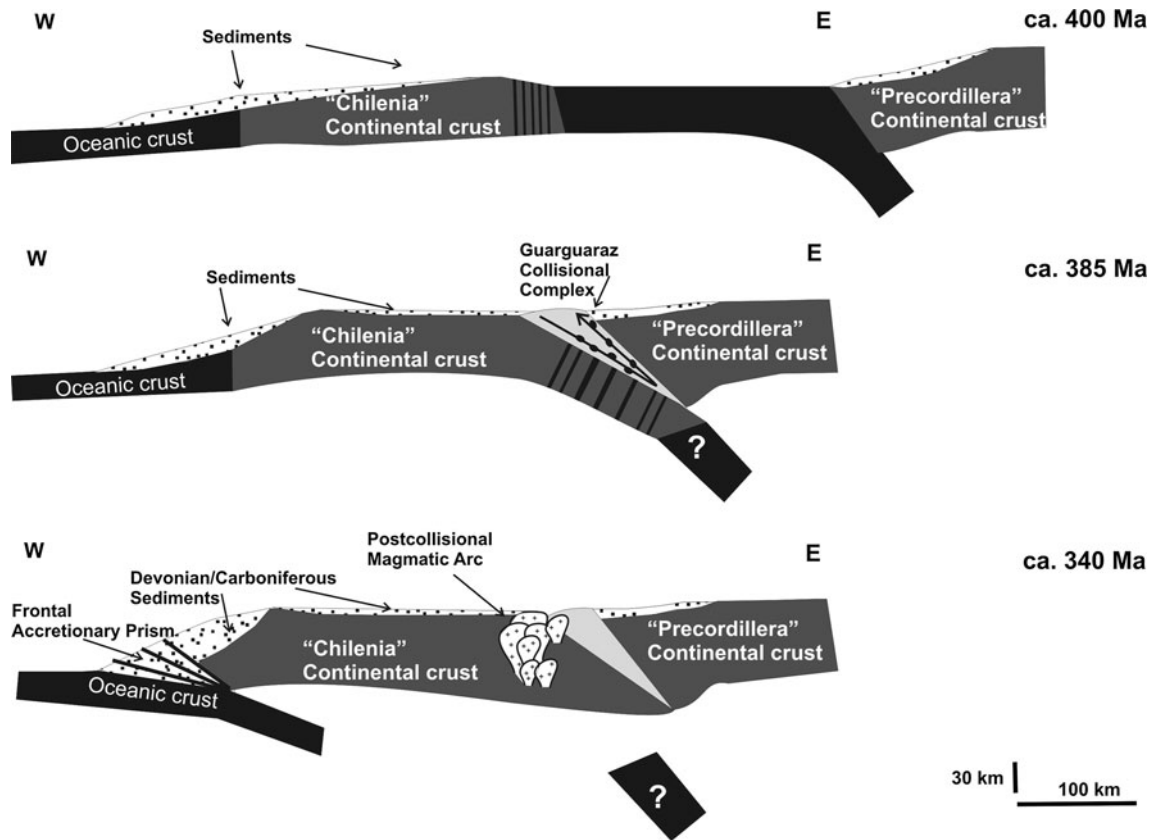


Fig. 10 EW cross-sections of the continental margin of South America showing the collision scenario of Chilenia at ca. 400–340 Ma

and thus exceeds maximum pressure at 0.8–1.1 GPa in the coastal accretionary prisms of Central Chile formed by basal accretion with metamorphic gradients around 12–15°C/km (Willner 2005). This is consistent with the observation that maximum depth of present accretionary prisms does not exceed 40 km (Ring and Brandon 1999) and most coastal accretionary prisms appear to evolve at metamorphic gradients exceeding 12°C/km (Massonne and Willner 2008). Furthermore, the average early minimum exhumation rates in the Guarguaraz Complex are significantly faster than in the coastal accretionary prisms.

3. Particularly, the decompression/heating path is of central importance for the recognition of collisional settings. In coastal accretionary systems such as the one of Central Chile, decompression during exhumation is always related to slight cooling (e.g. Willner 2005). On the other hand, decompression/heating paths are known from specific parts of the collision zones in continent–continent collisional belts such as the Alps (e.g. Bousquet 2008; Bousquet et al. 2008; Wiederkehr et al. 2009) and the Mid-European Variscides (e.g. Willner et al. 2000) as well as from numerical modelling of such settings (Willner et al. 2002; Gerya

et al. 2004; Faccenda et al. 2008). The significance of such PT paths is variable: (1) the pressure peak may be overprinted on a large scale by a later thermal peak at lower pressure due to radiogenic heat production, when large amounts of crustal material were accumulated in the collisional zone (e.g. Bousquet et al. 2008; Wiederkehr et al. 2009; Faccenda et al. 2008); (2) small volumes from the exhumation channel of a collisional complex may show decompression/heating paths, whereas neighbouring units show a mixture of heterogeneous PT evolutions, different maximum depths and interrelated PT paths (Willner et al. 2000, 2002; Bousquet 2008) and (3) heating during decompression may be due to thermal relaxation during exhumation of high-pressure/high-temperature rocks (Gerya et al. 2004). In the present case, there is not sufficient information, particularly of adjacent units to evaluate, which cause is valid for the present case.

The confirmed collisional belt is a further proof for the existence of the unexposed Chilenia Terrane. However, the assignment of the Guarguaraz Complex to either the Chilenia or the Cuyania Terrane depends on the original direction of dip of the collision zone which is currently a

matter of discussion. Because a magmatic arc prior to collision either did not develop or is not exposed, arguments for the direction of slab dip rely on structural arguments (Ramos et al. 1986; Davis et al. 1999). However, we would presently favour an east-dipping subduction zone with Chilenia and the Guararaz Complex as the lower plate (Fig. 10).

Conclusions

We describe the first comprehensive PTtd evolution, characterized by an overall clockwise path for the major rock types of the Guararaz Complex in part of a collision zone of a microplate in Andean South America. The characteristics for that environment become apparent when comparison is made with the evolution of coastal accretionary prisms as known from the Coastal Cordillera of Chile. These characteristics involve (1) burial of epicontinental sediments deposited long before the collision event in a basin outside its present position, (2) maximum pressure conditions exceeding 1.0 GPa by far under a metamorphic geotherm of 10–12°C/km, (3) early exhumation rates exceeding 1 mm/a and (4) a decompression/heating path. Such findings will also aid in the confirmation of real allochthonous terranes elsewhere in the future that have yet been proposed by different arguments for the Andes (Ramos 2009). However, to gain more insight into the mechanisms of collision zones, blocks from different depths must be studied in detail to derive interrelated PTtd paths.

The earliest geodynamic development in Central Chile is now well constrained (Fig. 10). After collision of Chilenia with Gondwana in Devonian times, a passive continental margin developed on the Pacific side of the microplate until it was converted into a convergent continental margin at about 340 Ma (Willner et al. 2009b) with the evolution of pronounced coastal accretionary systems and a late Palaeozoic paired metamorphic belt after ca. 300 Ma (Willner 2005, Willner et al. 2005).

Acknowledgments This work was financed by Deutsche Forschungsgemeinschaft (grant Ma1160/24) and the German–Chilean BMBF–CONICYT co-operation project (CHL07/025). Reviews by S.M. Kay and G. Topuz helped to improve this paper considerably. Careful editorial handling by T. Grove is acknowledged.

References

- Anczkiewicz R, Szczepański J, Mazur S, Storey C, Crowley Q, Villa IM, Thirlwall MF, Jeffries TE (2007) Lu-Hf geochronology and trace element distribution in garnet: implications for uplift and exhumation of ultra-high pressure granulites in the Sudetes, SW Poland. *Lithos* 95:363–380
- Astini R, Martina F, Ezpeleta M, Dávila F, Cawood P (2009) Chronology from rifting to foreland basin in the Paganzo Basin (Argentina), and a reappraisal on the “Eo- and Neohercynian” tectonics along Western Gondwana. *Abstracts XII Congreso Geológico Chileno Santiago* S9-010:179
- Basei M, Ramos VA, Vujovich GI, Poma St (1998) El basamento metamórfico de la Cordillera Frontal de Mendoza: nuevos datos geocronológicos e isotópicos. *Actas X Congreso Latinoamericano de Geología y VI Congreso Nacional de Geología Económica* II:412–417
- Berman RG (1988) Internally-consistent thermodynamic data for minerals in the system $\text{Na}_2\text{O}-\text{K}_2\text{O}-\text{CaO}-\text{MgO}-\text{FeO}-\text{Fe}_2\text{O}_3-\text{Al}_2\text{O}_3-\text{SiO}_2-\text{TiO}_2-\text{H}_2\text{O}-\text{CO}_2$. *J Petrol* 29:445–522
- Berman RG (1990) Mixing properties of Ca-Mg-Fe-Mn garnets. *Am Mineral* 75:328–344
- Bjerg EA, Gregori DA, Losada Calderón A, Labudía CH (1990) Las metamorfitas del faldeo oriental de la Cuchilla de Guararaz, Cordillera Frontal, Provincia de Mendoza. *Rev Asoc Geol Argent* 45:234–245
- Bousquet R (2008) Metamorphic heterogeneities within a same HP unit: overprint effect or metamorphic mix? *Lithos* 103:46–69
- Bousquet R, Oberhänsli R, Goffé B, Wiederkehr M, Koller F, Schmid SM, Schuster R, Engi M, Berger A, Martinotti G (2008) Metamorphism of metasediments in the scale of an orogen: a key to the tertiary geodynamic evolution of the Alps. In: Siegesmund S, Fügenschuh, B, Froitzheim N (eds) *Tectonic aspects of the alpine-dinaride-carpathian system*. Geological Society, London, Special Publications 298:393–412
- Brix MR, Stöckert B, Seidel E, Theye T, Thomson SN, Küster M (2002) Thermobarometric data from a fossil zircon partial annealing zone in high pressure-low temperature rocks of eastern and central Crete, Greece. *Tectonophysics* 349:309–326
- Brown TH, Berman RG, Perkins EH (1989) Ge0-Calc: software package for calculation and display of pressure-temperature-composition phase diagrams using an IBM or compatible personal computer. *Comput Geosci* 14:279–289
- Caminos R (1979) Cordillera frontal. *Segundo Simp Geol Reg Argent* 1:397–454
- Caminos R (1993) El basamento metamórfico proterozoico-paleozoico inferior. In: Ramos VA (ed) *Geología y recursos naturales de Mendoza. 12. Congreso Geológico Argentino y 2. Congreso de Exploración de Hidrocarburos*, Buenos Aires, Relatorio 1:11–19
- Caminos R, Cordani U, Linares E (1979) Geología y geocronología de las rocas metamórficas y eruptivas de la Precordillera y Cordillera Frontal de Mendoza. *Actas 2. Congreso Geológico Chileno Santiago* 1:43–61
- Connolly JAD (1990) Multivariable phase diagrams; an algorithm based on generalized thermodynamics. *Am J Sci* 290:666–718
- Connolly JAD (2005) Computation of phase equilibria by linear programming: a tool for geodynamic modeling and its application to subduction zone decarbonation. *Earth Planet Sci Lett* 236:524–541
- Davis J, Roeske S, McClelland W, Snee L (1999) Closing the ocean between the Precordillera terrane and Chilenia: early Devonian ophiolite emplacement and deformation in the southwest Precordillera. In: Ramos VA, Keppie J (eds) Laurentia and Gondwana connections before Pangea. *Geol Soc Am Spec Paper* 336:115–138
- Davis J, Roeske S, McClelland W, Kay SM (2000) Implications of mafic and ultramafic crustal fragments of the SW Precordillera terrane for early Paleozoic tectonic models of Western Argentina. *Geology* 28:171–174
- Evans BW (1990) Phase relations of epidote-blueschists. *Lithos* 24:3–23
- Faccenda M, Gerya TV, Chakraborty S (2008) Styles of postsubduction collisional orogeny: influence of convergence velocity,

- crustal rheology and radiogenic heat production. *Lithos* 103:257–287
- Fuhrman ML, Lindsley DH (1988) Ternary feldspar modeling such features are of continental extent and must be due and thermometry. *Am Mineral* 73:201–215
- Galbraith RF, Laslett GM (1993) Statistical models for mixed fission track ages. *Nucl Tracks* 21:459–470
- Gerbi C, Roeske SM, Davis JS (2002) Geology and structural history of the southwest Precordillera margin, northern Mendoza Province, Argentina. *J South Am Earth Sci* 14:821–835
- Gerya TV, Perchuk LL, Maresch WV, Willner AP (2004) Inherent gravitational instability of hot continental crust: implication for doming and diapirism in granulite facies terrains. In: Whitney DI, Teyssier C, Siddoway CS (eds) *Gneiss domes in orogeny*. *Geol Soc Am Spec Paper* 380:97–115
- Glodny J, Lohrmann J, Echtler H, Gräfe K, Seifert W, Collao S, Figueira O (2005) Internal dynamics of a paleoaccretionary wedge: insights from combined isotope tectonochronology and sandbox modelling of the south-central Chilean fore-arc. *Earth Planet Sci Lett* 231:23–39
- Gregori DA, Fernandez-Turiel JL, Lopez-Soler A, Petford N (1996) Geochemistry of Upper Palaeozoic-Lower Triassic granitoids of the Central Frontal Cordillera (33°10–33°45), Argentina. *J South Am Earth Sci* 9:141–151
- Hervé F (1988) Late Paleozoic subduction and accretion in Southern Chile. *Episodes* 11:183–188
- Holland TJB, Powell R (1998) An internally consistent thermodynamic data set for phases of petrological interest. *J Metamorphic Geol* 16:309–343
- Holland TJB, Powell R (2003) Activity-composition relations for phases in petrological calculations: an asymmetric multicomponent formulation. *Contrib Mineral Petrol* 145:492–501
- Hurford AJ (1990) Standardization of fission track dating calibration: recommended by the Fission Track Working Group of the I.U.G.S. Subcommission on Geochronology. *Chem Geol (Isot Geosci Sect)* 80:171–178
- Hurford AJ, Green PF (1983) The zeta age calibration of fission-track dating. *Isotope Geosci* 1:285–317
- Ishizuka O, Yuasa M, Uto K (2002) Evidence of porphyry copper-type hydrothermal activity from a submerged remnant back-arc volcano of the Izu-Bonin arc: implication for the volcanotectonic history of back-arc seamounts. *Earth Planet Sci Lett* 198:381–399
- Konrad-Schmolke M, Zack TH, O'Brien PJ, Jacob DE (2008) Combined thermodynamic and rare earth element modelling of garnet growth during subduction: examples from ultrahigh-pressure eclogite of the Western Gneiss Region, Norway. *Earth Planet Sci Lett* 272:488–498
- Lagos M, Scherer EE, Tomaschek F, Münker C, Keiter M, Berndt J, Baumann C (2007) High precision Lu-Hf geochronology of Eocene eclogite-facies rocks from Syros, Cyclades, Greece. *Chem Geol* 243:16–35
- Lopez VL, Gregori DA (2004) Provenance and evolution of the Guararaz Complex, Cordillera Frontal, Argentina. *Gondwana Res* 7:1197–1208
- Lopez VL, Escayola M, Azarevich MB, Pimentel MM, Tassinari C (2009) The Guararaz Complex and the Neoproterozoic-Cambrian evolution of southwestern Gondwana: geochemical signatures and geochronological constraints. *J South Am Earth Sci* 28:333–344
- Ludwig K (2007) Isoplot/Ex version 3.41b, a geochronological toolkit for Microsoft Excel. Berkeley Geochronology Center Special Publication No. 4
- Massonne HJ (1995a) Experimental and petrogenetic study of UHPM. In: Coleman RG, Wang X (eds) *Ultrahigh pressure metamorphism*. Cambridge University Press, Cambridge, pp 33–95
- Massonne HJ (1995b) P-T evolution of metavolcanics from the southern Taunus mountains. In: Dallmeyer RD, Franke W, Weber K (eds) *Pre-permian geology of central and eastern Europe*. Springer, Berlin-Heidelberg, pp 132–137
- Massonne HJ (1997) An improved thermodynamic solid solution model for natural white-micas and its application to the geothermobarometry of metamorphic rocks. *Geological Survey of Finland Guide* 46, Mineral equilibria and databases, Abstracts:49
- Massonne HJ, Calderón M (2008) P-T evolution of metapelites from the Guararaz Complex, Argentina: evidence for Devonian crustal thickening close to the western Gondwana margin. *Rev Geol Chile* 35:215–231
- Massonne HJ, Szpurka Z (1997) Thermodynamic properties of white-mica on the basis of high-pressure experiments in the systems $K_2O-MgO-Al_2O_3-Si_2O-H_2O$ and $K_2O-FeO-Al_2O_3-Si_2O-H_2O$. *Lithos* 41:229–250
- Massonne HJ, Willner AP (2008) Phase relations and dehydration behaviour of psammopelite and mid-ocean ridge basalt at very-low-grade to low-grade metamorphic conditions. *Eur J Mineral* 20:867–879
- McDougall I, Harrison TM (1999) *Geochronology and thermochronology by the $^{40}Ar/^{39}Ar$ -method*. Oxford University Press, Oxford, 269 pp
- McMullin DW, Berman RG, Greenwood HJ (1991) Calibration of the SGAM thermometer for pelitic rocks using data from equilibrium experiments and natural assemblages. *Can Mineral* 29:889–908
- Mpodozis C, Kay SM (1992) Late Paleozoic to Triassic evolution of the Gondwana margin: evidence from Chilean Cordilleran batholiths (28°–31°S). *Bull Geol Soc Am* 104:999–1024
- Münker C, Weyer S, Scherer EE, Mezger K (2001) Separation of high field strength elements (Nb, Ta, Zr, Hf) and Lu from rock samples for MC-ICPMS measurements. *Geochem Geophys Geosyst*. doi:[10.1029/2001GC000183](https://doi.org/10.1029/2001GC000183) (G3) 2
- Ogg JG, Ogg G, Gradstein FM (2008) *The concise geological time scale*. Cambridge University Press, Cambridge, 177 pp
- Patchett PJ, Tatsumoto M (1980) A routine high-precision method for Lu-Hf isotope geochemistry and geochronology. *Contrib Mineral Petro* 75:263–267
- Polanski J (1964) Descripción Geológica de la Hoja 24^a-b Cerro Tupungato (Provincia de Mendoza). Dirección Nacional de Geología y Minería, Boletín 98: 94 p. Buenos Aires
- Polanski J (1972) Descripción Geológica de la Hoja 25a Volcán San José (Provincia de Mendoza). Dirección Nacional de Geología y Minería, Boletín 128: 114 p. Buenos Aires
- Powell R, Holland TJB (1999) Relating formulations of the thermodynamics of mineral solid solutionns: activity modeling of pyroxenes, amphiboles and micas. *Am Mineral* 84:1–14
- Rahn M, Brandon M, Batt GE, Garver JI (2004) A zero-damage model for fission-track annealing in zircon. *Am Mineral* 89:473–484
- Ramírez-Sánchez E, Deckart K, Hervé F (2007) Significance of $^{40}Ar/^{39}Ar$ encapsulation ages of metapelites from late Palaeozoic metamorphic complexes of Aysén, Chile. *Geol Mag* 145:389–396
- Ramos VA (2000) The southern central Andes. In: Cordani UG, Milani EJ, Thomaz Filho, A, Campos DA (eds) *Tectonic evolution of South America*. Inter Geol Congress Rio de Janeiro 561–604, 31
- Ramos VA (2009) Anatomy and global context of the Andes: main geologic features and the Andean orogenic cycle. In: Kay SM, Ramos VA, Dickinson WR (eds) *Backbone of the Americas: shallow subduction, plateau uplift, and ridge and terrane collision*. *Geol Soc Am Memoir* 204:31–65
- Ramos VA, Jordan TE, Allmendinger RW, Mpodozis C, Kay SM, Cortés JM, Palma MA (1986) Paleozoic terrains of the central Argentine Chilean Andes. *Tectonics* 5:855–880

- Richter PP, Ring U, Willner AP, Leiss B (2007) Structural contacts in subduction complexes and their tectonic significance: the late Palaeozoic coastal accretionary wedge of central Chile. *J Geol Soc London* 164:203–214
- Ring U, Brandon MT (1999) Ductile deformation and mass loss in the Franciscan subduction complex: implications for exhumation processes in accretionary wedges. In: Ring U, Brandon MT, Lister GS, Willett SD (eds) *Exhumation processes: normal faulting, ductile flow and erosion*. *Geol Soc London Spec Publ* 154:55–86
- Ruviños MA, Gregori DA, Bjerg EA (1997) Condiciones de P y T del basamento metamórfico de la Cordillera Frontal de Mendoza, Argentina. *Actas 8. Congreso Geológico Chileno Antofagasta* 2:1512–1516
- Scherer EE, Cameron KL, Blichert-Toft J (2000) Lu–Hf garnet geochronology: closure temperature relative to the Sm–Nd system and the effects of trace mineral inclusions. *Geochim Cosmochim Acta* 64:3413–3432
- Scherer E, Münker C, Mezger K (2001) Calibration of the lutetium–hafnium clock. *Science* 293:683–687
- Schmidt A, Weyer S, Mezger K, Scherer EE, Yilin X, Hoefs J, Brey G (2008) Rapid eclogitisation of the Dabie-Sulu UHP terrane: constraints from Lu-Hf garnet geochronology. *Earth Planet Sci Lett* 273:203–213
- Skora S, Baumgartner LP, Mahlen NJ, Johnson CM, Pilet S, Hellebrand E (2006) Diffusion-limited REE uptake by eclogite garnets and its consequences for Lu-Hf and Sm-Nd geochronology. *Contrib Mineral Petro* 152:703–720
- Söderlund U, Patchett PJ, Vervoort JD, Isachsen CE (2004) The ^{176}Lu decay constant determined by Lu–Hf and U–Pb isotope systematics of Precambrian mafic intrusions. *Earth Planet Sci Lett* 219:311–324
- Tagami T, Galbraith RF, Yamada R, Laslett GM (1998) Revised annealing kinetics of fission tracks in zircon and geological implications. In: Van den Haute P, De Corte F (eds) *Advances in fission-track geochronology*. Kluwer Academic Publishers, Dordrecht, pp 99–112
- Thomson SN, Ring U (2006) Thermochronologic evaluation of postcollision extension in the Anatolide Orogen, western Turkey. *Tectonics* 25:TC3005. doi:[10.1029/2005TC001833](https://doi.org/10.1029/2005TC001833)
- Uto K, Ishizuka O, Matsumoto A, Kamioka H, Togashi S (1997) Laser-heating $^{40}\text{Ar}/^{39}\text{Ar}$ dating system of the Geological Survey of Japan: system outlines and preliminary results. *Bull Geol Surv Jpn* 48:23–46
- Villa IM (1998) Isotopic closure. *Terra Nova* 10:42–47
- Vujovich GI, Gregori D (2002) Cordón del Portillo, Cordillera Frontal, Mendoza: Caracterización geoquímica de las metamorfitas. *Actas 15. Congreso Geológico Argentino Calafate:1–6*
- Wiederkehr M, Sudo M, Bousquet R, Berger A, Schmid SM (2009) Alpine orogenic evolution from subduction to collisional thermal overprint: the $^{40}\text{Ar}/^{39}\text{Ar}$ age constraints from the Valaisan Ocean, Central Alps *Tectonics* 28:TC6009. doi:[10.1029/2009TC002496](https://doi.org/10.1029/2009TC002496)
- Willner AP (2005) Pressure-temperature evolution of an Upper Paleozoic paired metamorphic belt in Central Chile (34° – 35° 30'S). *Journal of Petrology* 46:1805–1833
- Willner AP, Krohe A, Maresch WV (2000) Interrelated PTtd-paths in the Variscan Erzgebirge Dome (Saxony/Germany): constraints for the rapid exhumation dynamics of HP-HT rocks from the root zone of a collisional orogen. *Int Geol Rev* 42:64–85
- Willner AP, Sebazungu E, Gerya TV, Maresch WV, Krohe A (2002) Numerical modeling of PT-paths related to rapid exhumation of high-pressure rocks from the crustal root in the Variscan Erzgebirge Dome Saxony/Germany. *J Geodyn* 33:281–314
- Willner AP, Thomson SN, Kröner A, Wartho JA, Wijbrans J, Hervé F (2005) Time markers for the evolution and exhumation history of a late Palaeozoic paired metamorphic belt in central Chile (34° – 35° 30'S). *J Petrol* 46:1835–1858
- Willner AP, Gerdes A, Massonne HJ (2008) History of crustal growth and recycling at the Pacific convergent margin of South America at latitudes 29° – 36° S revealed by a U-Pb and Lu-Hf isotope study of detrital zircon from late Paleozoic accretionary systems. *Chem Geol* 253:114–129
- Willner AP, Sepúlveda FA, Hervé F, Massonne HJ, Sudo M (2009a) Conditions and timing of pumpellyite–actinolite facies metamorphism in the Early Mesozoic frontal accretionary prism of the Madre de Dios Archipelago (50° 20'S; S-Chile). *J Petrol* 50:2127–2155
- Willner AP, Massonne HJ, Gerdes A, Hervé F, Sudo M, Thomson S (2009b) The contrasting evolution of collisional and coastal accretionary systems between the latitudes 30° S and 35° S: evidence for the existence of a Chilenia microplate. *Abstracts XII Congreso Geológico Chileno Santiago S9_099:223*